

Impacts on the Moon: analysis methods and size distribution of impactors.

Chrysa Avdellidou^{a,b,*}, Edhah Munaibari^{c,b}, Raven Larson^d, Jeremie Vaubaillon^e, Marco Delbo^a, Paul Hayne^d, Mark Wieczorek^a, Daniel Sheward^f, Antony Cook^f

^aUniversité Côte d'Azur, CNRS, Observatoire de la Côte d'Azur, Laboratoire Lagrange, Blvd de l'Observatoire, CS 34229, 06304 Nice cedex 4, France

^bUniversité Côte d'Azur, CNRS, Observatoire de la Côte d'Azur, Géoazur, 250 rue Albert Einstein, Sophia Antipolis 06560 Valbonne, France

^cMaster of Astrophysics - Université Côte d'Azur (MAUCA), Dépt. de Physique (Campus Sciences, UCA) & Observatoire de la Côte d'Azur, Parc Valrose, 06100 Nice, France

^dLaboratory for Atmospheric and Space Physics, and Astrophysical & Planetary Sciences Department, University of Colorado Boulder, Boulder, CO, USA

^eInstitut de Mécanique Céleste et de Calcul des Ephémérides, Observatoire de Paris/PSL, 77 Av Denfert Rochereau, F-75014 Paris, France

^fDepartment of Physics, Aberystwyth University, Ceredigion, United Kingdom, SY23 3BZ

Abstract

We are preparing a telescope system to carry out a survey of detection and analysis of lunar impact flashes. In the framework of this project, here we present all necessary methods to automatically identify these luminous events, their lunar impact coordinates, the origin of the impacting meteoroids, as well as the estimation of their physical properties such as mass and size. We tested our methods against confirmed impact events and constructed the meteoroid size frequency distribution of impactors using literature data of the last 20 years. In addition, we present the first lunar impact event observed from the Observatoire de la Côte d'Azur that was detected during the testing phase of our project.

Keywords: Moon, surface, Impact processes, Meteoroids

2010 MSC: 00-01, 99-00

*Corresponding author

1. Introduction

Impact cratering is a fundamental process, altering planetary surfaces. Currently we have reached a level where we observe and study impact craters on a plethora of solar system bodies such as planets, moons, asteroids (Marchi et al., 2015, 2012; Sugita et al., 2019; Walsh et al., 2019), Kuiper-belt objects (Singer et al., 2019) and comet nuclei (Vincent et al., 2015). Cratering has been used, together with the knowledge of the size frequency distribution of potential impactors for a given collisional environment, in order to date planetary surfaces based on the simple idea that old surfaces have accumulated more impact craters than more recent ones. This started more than 50 years ago with the Moon (Baldwin, 1971) and was later used to study the chronology on other planetary surfaces such as Mercury (Neukum et al., 2001), Venus (Korycansky & Zahnle, 2005), and Mars (Ivanov, 2001; Hartmann & Neukum, 2001). At the same time impact scaling laws have also been developed (e.g. Schmidt & Housen, 1987; Holsapple, 1994). Impact craters have been observed at different scales that span from kilometres, on planetary surfaces, down to microns, as for example on the returned lunar samples. NASA's sample return space mission OSIRIS-REx has recorded *in situ* impact craters on the boulders of the target near-Earth asteroid (101955) Bennu, covering a range from 3 cm up to 5 m (Ballouz et al., 2020).

In parallel, laboratory experiments have advanced on the type of materials that are used to simulate planetary surfaces (Daly & Schultz, 2015, 2016; Avdellidou et al., 2016, 2017, 2020; Flynn et al., 2018, 2020). During laboratory experiments we are able to control and have accurate measurements of the mass, size and velocity of the impactor in order to study the crater formation. However, the size scales and velocity ranges (and thus the energy) are smaller than in planetary scales. On the other hand, at larger planetary scales

cratering is mainly studied at a later time of the impact and there is no absolute link between the impacting body and the formed crater. In this respect there have been executed several large-scale experiments of artificial impacts on planetary surfaces. Throughout the decades spacecraft on lunar orbits have eventually crashed on the Moon producing craters, several of which are identified and studied especially with the help of Lunar Reconnaissance Orbiter's (LRO) data (Plescia et al., 2016). One of those anthropogenic impacts was ESA's SMART-1 (Foing et al., 2018) whose crater was detected years later in the LRO data (Stooke, 2019) and NASA's LCROSS (Colaprete et al., 2010; Schultz et al., 2010) whose impact was observed by the LRO/Diviner (Hayne et al., 2010) as well as from the Earth (Strycker et al., 2013). On the nucleus of comet 9P/Tempel was performed the Deep Impact experiment by the Stardust-NExT mission that allowed the observation of the ejecta evolution at a real time (Schultz et al., 2007) but also later (Schultz et al., 2013). In 2019 the Small Carry-on Impactor (SCI) of JAXA's Hayabusa2 sample return mission hit the surface of its target near-Earth asteroid (162173) Ryugu (Arakawa et al., 2020), while a new large scale impact experiment is being prepared on Dimorphos, the satellite of near-Earth asteroid (65803) Didymos, by NASA's DART mission in 2022 (Cheng et al., 2016). In several cases laboratory impact studies have been done in order to accompany the aforementioned artificial experiments (see for example Schultz et al., 2005; Burchell et al., 2015).

In this respect, since late 90s, the lunar surface has been monitored in order to detect transient light phenomena that occur during meteoroid hypervelocity impact events, and we refer to these events as lunar impact flashes (LIF). These observations have been performed by small and moderate telescopes from the ground with the aim to derive the impact flux of cm- to dm-sized meteoroids (Suggs et al., 2014; Ait Moulay Larbi et al., 2015; Bonanos et al., 2018; Avdelli-

dou & Vaubaillon, 2019). In parallel, several detection and analysis techniques have been developed depending on the specific observational setup (single or double camera systems) and the scientific goals of the teams (Bouley et al., 2012; Madiedo et al., 2015b; Xilouris et al., 2018). In a few cases NASA’s Lunar Reconnaissance Orbiter (LRO) has detected these impact craters on the lunar surface (Suggs et al., 2014; Robinson et al., 2015; Ortiz et al., 2015).

In this work we use current techniques of lunar observations and develop a methodology to observe and study live impacts of cm to dm-size impactors in space. For our project the surface of the Moon provides an excellent opportunity because it is the closest planetary body to Earth; it suffers impacts from known populations of cm to dm-size objects (when they are linked to meteoroid streams, but less certain for the sporadic meteoroids); lunar orbiters provide data for crater detection; and low-cost instrumentation can be used worldwide for a continuous monitoring of the lunar surface. Additional advantage of observing impacts on an atmosphere-less body such as the Moon is that the impacting object is allowed to reach the lunar surface without breaking. In that way we could estimate its original size and establish a link between the impacting meteoroid and the produced crater. At the same time meteoroid impacts on planetary objects with atmosphere provide complementary advantages such as the estimation of their strength and density, the latter crucial parameter for size estimation techniques, as will also be presented later in this work. The lunar impactors we intend to study here have small sizes and velocities that, if originate from meteoroid streams, can reach up to 70 km s^{-1} , while at their lower end, coming from asteroid orbits Bottke et al. (2002), their impact velocity distribution has a maximum at about 12 km s^{-1} allowing velocities down to $\sim 5 \text{ km s}^{-1}$ Le Feuvre & Wieczorek (2011). In a broader picture we can consider those impacts are an extension in size and energy scales of the current laboratory

impact experiments using light-gas guns, where masses are up to a few grams and velocities limited to $\sim 8 \text{ km s}^{-1}$.

We are building a new observational collaborative survey in order to observe the lunar surface starting from two sites, in France and the UK. Our scientific goal is to perform statistics of the meteoroids regarding their size frequency distribution and subsequently detect their craters, establishing a link between the size of the crater and the impactor. In addition, we want to study differences in physical properties between the different population of the impactors (different meteoroid streams which are known to have different composition and material density) as well as the cooling rate of the molten lunar regolith, hunting for differences between impacts on maria vs. highlands. In those two lunar soils the grain size of the regolith is the same, but the mineralogy differs from basalt to anorthosite respectively.

We collected LIFs from the literature, which are used for two purposes: (i) as input to build our LIF analysis methods and (ii) to construct the size frequency distribution of small meteoroids that hit the Moon. In addition, we have performed our own test observations and built our custom LIF detection algorithm. Specifically in § 2 we present the datasets that we used for our analysis, in § 3 we describe our methods to identify potential LIFs in observational data. In § 4 we describe in detail how we derive the selenographic coordinates of the events and in § 5 how we identify the origin of each meteoroid impactor. The estimation of the mass and size of the impactors is presented in § 6. In § 7 we report our first detection that was observed during the testing phase of the project and finally in § 8 we discuss our results.

2. Data

For the purposes of this work we use the publicly available data that were acquired in the last two decades and obtained from scientific publications or official websites. More specifically, we tested the performance of our algorithms on the NELIOTA dataset, while all the datasets presented below were used to derive the size frequency distribution of the impacting meteoroids.

2.1. NELIOTA

The ESA-funded program NELIOTA run at the National Observatory of Athens with a goal to detect LIFs. As of December 1st 2020 there have been detected, by NELIOTA's double camera system, 112 confirmed LIFs in about 167 hours of observations since February 1st 2017, giving a rate of 1 flash every 1.5 hours of observations. Extensive details on the instrumentation, the observational method and calibration techniques are given by Xilouris et al. (2018) and Bonanos et al. (2018). The NELIOTA website¹ provides data for the date and time of each event (Tab. 3), selenographic coordinates (Tab. A.5), duration and the calibrated peak magnitudes in *R* and *I* bands. Unfortunately, as it is derived by Xilouris et al. (2018) and Liakos et al. (2020), the reported magnitudes and errors on the NELIOTA database are approximate, while some selenographic coordinates are possibly reported incorrectly (swapped longitude and latitude). In this work, for the flashes with numbers 1-80 we use the published magnitudes and selenographic coordinates (Xilouris et al., 2018; Liakos et al., 2020), while for the rest (81-112) we use the data as reported on the website. As we will see later, we use our method and re-compute the selenographic coordinates (Tab. A.5), which we use for the rest of the analysis. Additionally, we retrieved the datacubes that include the total frames in which a flash appears. These were

¹neliota.astro.noa.gr

used in order to estimate the R and I magnitudes of the subsequent frames in the multi-frame events (Avdellidou & Vaubaillon, 2019).

2.2. Marshall Space Flight Center

Since 2006, NASA’s Marshall Space Flight Center (MSFC), has started an observational program, which monitors the lunar surface, hunting for LIFs. Observations are conducted at NASA Marshall Space Flight Center in Huntsville, Alabama at the Automated Lunar and Meteor Observatory (ALaMO). Detailed description on their instrumentation and observational methods can be found in Suggs et al. (2014). Until 2018 435 LIF detections had been published online², however, in this work we will use only the published data (126 events) by Suggs et al. (2014). This dataset contains information about the date, time, solar longitude, R magnitude, selenographic coordinates (Tab. A.5) and luminous energy (Tab. 3). The reason for which we did not use the full online dataset is that no magnitude information is provided, and thus no further analysis could be done for our purposes.

2.3. Other observations

Apart from the two aforementioned surveys there are numerous LIF observations that were done by different teams in Spain (Ortiz et al., 2002, 2006, 2015; Madiedo et al., 2015a,b, 2016, 2018), Japan (Yanagisawa & Kisaichi, 2002; Yanagisawa et al., 2006), USA (Dunham et al., 2000; Cudnik et al., 2003), Morocco (Ait Moulay Larbi et al., 2015) and Mexico (Ortiz et al., 2000) using small telescopes with diameters between 20 and 40 cm. From all these studies we have collected the date and time (Tab. 3), impact duration, magnitude and selenographic coordinates for 69 events in total (Tab. 3). The luminous energy was given only for five events (Ait Moulay Larbi et al., 2015).

²https://www.nasa.gov/centers_marshall/news/lunar/lunar_impacts.html

3. Detection of events

The first step is to identify all the potential LIF events in the datasets of the observations. We developed two approaches that can be used to carry out real time detection of LIFs. Both approaches are based on the creation of a master reference frame, which we call the Lunar Background (LB), that is subtracted from all frames of the night side of the Moon. This is necessary in order to remove the inhomogeneous surface of the Moon and the earthshine. From each frame we subtract a LB that is created by the median combination of the 10 previous frames and thus any potential luminous transient phenomenon should remain in the images. This analysis step will be carried out synchronously with the observations and the data acquisition of our developing observing system.

In the first detecting method we apply a threshold on the pixel values of the background-subtracted frames. Then, to ensure that all the pixels detected to be above the threshold are not due to any artefacts, we developed and applied multiple filters. This is to confirm that the pixels of a LIF form a Gaussian shape. As this method is based on the application of a threshold, a careful selection of the values of those criteria is required, as larger values can result on missing fainter impacts and lower values may increase the number of detected artefacts (false detection).

The second method, is to apply a Gaussian filter to the background-subtracted images. This will smooth most of the artefacts leading to their elimination. In this case we do not need to apply cleaning filters (as in the first approach) saving computational time. This process will enhance the pixels of a potential event which leads to an easy detection even for faint LIFs. In that way we overcome the issue of incorrect selection of any threshold, as described in the first method.

The most significant consideration when developing these real-time detection methods was the fast execution and the short computational time in order to

keep up with the running observations. Both methods were tested against data containing synthetic LIFs that we generated, as well as against the archived data from NELIOTA. The results of our examination show that both approaches can keep up with real time observations, detect all events (real or simulated) with the first approach being faster but less sensitive to fainter LIFs.

4. Selenographic Coordinates

The importance of accurately locating the selenographic latitude and longitude (β, λ) of a LIF comes from the fact that it is needed to perform the process of linking the impactor to its source. Moreover, it allows us to investigate the aftermath of an impact, by searching for the produced crater or the fresh ejecta deposits using spacecraft data from the LRO (Sheward et al., 2019).

As mentioned before, the selenographic coordinates of the confirmed LIFs are also reported in the literature (Tab. A.5). For the sake of our preliminary survey, we have developed the Automated Geolocation of Lunar Surface Impacts (AUGUR) algorithm to identify the selenographic coordinates from individual observations (Larson et al., 2019). In order to test AUGUR’s performance we applied it to the NELIOTA events, as it is the only survey that provides access to the complete datacube of each detection, in the form of FITS files.

The AUGUR algorithm takes in images, containing a LIF, and returns the selenographic coordinates of that impact and its respective error. Once an impact flash is detected in an image, AUGUR can be automatically triggered to geolocate the selenographic coordinates of that flash. Fig. 1 shows the full mechanics of the AUGUR algorithm, however, this will be broken down into the three main steps of image reduction, image correlation, and coordinate transformation.

Before AUGUR begins the image reduction and correlation, it first uses the

JPL Horizons database to pull information to generate a projection of the Moon for each observation. This projection uses an orthographic projection matrix and takes into account lunar librations by setting the sub-observer latitude and longitude as the (0,0) coordinate for the projection. The projection is wrapped with the *Moon LRO LROC WAC Global Morphology Mosaic* to build a projected Moon that can later be used by AUGUR during image correlation. AUGUR performs best when provided a datacube of a minimum 10 lunar images, which should contain the lunar limb. Terminator could be contained as well.

The first step of AUGUR is to reduce the image data. Once the datacube is loaded into AUGUR, it is essential to stack the images to bring out as many lunar features as possible. Since the images are taken using a high speed imaging system, distortion in between frames is negligible and they can be stacked without temporal alignment. After the images are stacked, it is then necessary to remove the light gradient coming from the terminator of the Moon or from any Earthshine presented in the image. This can be done by putting the stacked image through a low-pass filter, thus preserving the lunar features but removing the saturation of excess light in the images. For a low-pass filter AUGUR applies a large Gaussian blur ($\sigma = 25$ pxl) to the stacked image by calculating a Gaussian filter kernel using

$$G(x, y) = \frac{1}{2\pi\sigma^2} e^{-\frac{x^2+y^2}{2\sigma^2}} \quad (1)$$

where σ is the standard deviation of the Gaussian, and (x, y) are the pixel coordinates of the image. We can then convolve that kernel with the original stacked image using

$$V = \left| \frac{\sum_{x=0}^{\sigma} (\sum_{y=0}^{\sigma} G_{xy} d_{xy})}{F} \right| \quad (2)$$

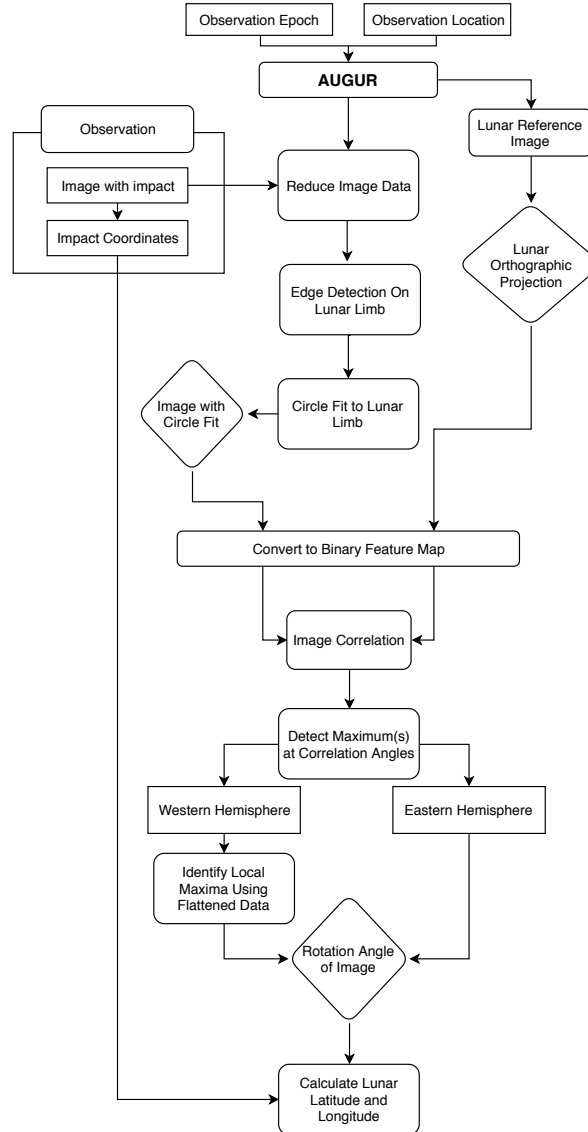
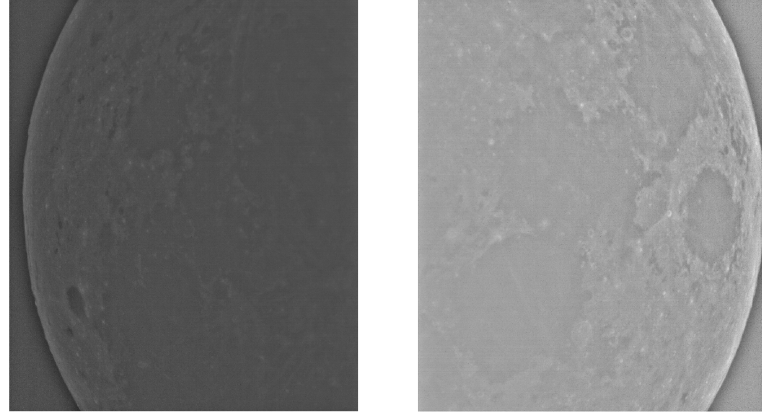


Figure 1: The full process of the AUGUR algorithm. Rectangular boxes are inputs to the program and diamond boxes are outputs.



(a) Western

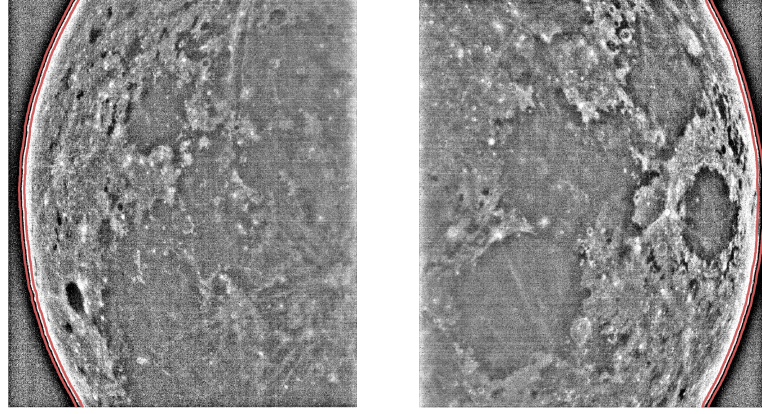
(b) Eastern

Figure 2: Results of the stacked image being sent through a low-pass filter to remove the light gradient but preserve the lunar features. Both of these images were taken at an illumination of 21% – 22% resulting in good feature preservation after the light gradient was removed. Images taken from the NELIOTA website.

where d_{xy} is the data value of the pixel, and F is the sum of the coefficients within the kernel (this is set to 1 if the sum of the coefficients is 0). Once the Gaussian blur is applied to the stacked image, the light gradient is all that remains. To remove the light gradient from the stacked image, we divide the stacked image by the blurred image to leave only the lunar features. The result of this low-pass filter can be seen in Fig. 2.

The next step is to automate the detection of the lunar limb in the reduced images. This is later needed to align the image with the projected Moon and correlate where the image is located within the lunar hemisphere. To detect the lunar limb, the image is run through a Sobel filter to enhance the lunar limb from the background. The Sobel filter method is similar to the low-pass filter method laid out above in that it passes the image through a Gaussian filter and then convolves that kernel with the original image. However, the Sobel filter requires a smaller Gaussian blur effect and uses a 3×3 ($\sigma = 3$ pixels) kernel.

The Sobel edge detection uses two convolution kernels (G_x, G_y) with one



(a) Western

(b) Eastern

Figure 3: Light gradient removed images with the inner and out edge of the lunar limb detected (red). The average of these two detections is used for the final location of the lunar limb, resulting in ~ 1 pixel accuracy. These images do not represent the magnitudes of the Sobel filter but are instead the light gradient removed images with a pixel threshold applied to them for contrast. Images taken from the NELIOTA website.

detecting change in the x-direction of the image and the other detecting change in the y-direction of the image. The G_x kernel is simply the G_y kernel rotated by 90 degrees. To detect the lunar limb, the magnitudes of the kernels are calculated using

$$|G_{mag}| = \sqrt{G_x^2 + G_y^2}. \quad (3)$$

The higher resulting magnitudes correspond with a larger gradient change in the pixel grid. AUGUR then locates pixels that correspond to higher magnitudes and saves them as the potential x and y coordinate pairs of the lunar limb, as seen in Fig. 3.

After the detection of the lunar limb is complete (with ~ 1 pxl accuracy), a circle can be fit to the limb with a least squares circle fit method using

$$g(u, v) = (u - u_c)^2 + (v - v_c)^2 - \alpha \quad (4a)$$

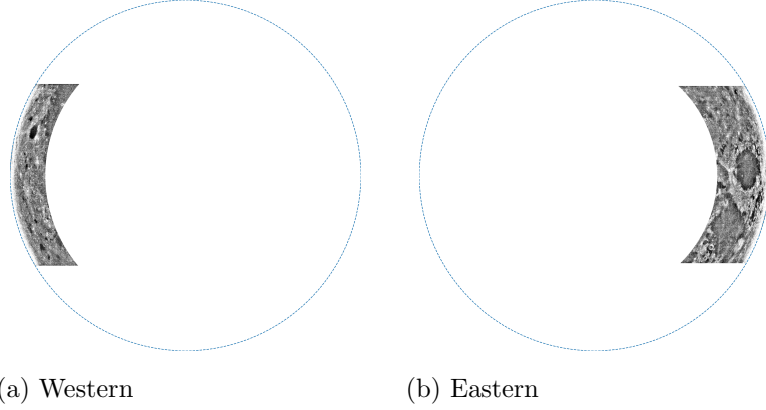


Figure 4: The masked images with their corresponding least-squares circle fit. Images in the Western of the Moon are masked to show 20% of the image, and images on the Eastern hemisphere are masked to show 30%. This is to deter AUGUR from a false rotation angle detection by focusing near the lunar limb where the contrast for the lunar features is more prominent. AUGUR best identifies Grimaldi crater for the Western hemisphere and Mare Crisium for the Eastern. Images taken from the NELIOTA website.

and

$$S = \sum_i (g(u_i, v_i))^2 \quad (4b)$$

where $\alpha = R^2$ and $u_c, v_c = (x_c, y_c) - (\bar{x}, \bar{y})$ provides the central coordinates of the best fit circle in the original (x, y) coordinate system of the image, assuming $u_i = x_i - \bar{x}$, and $v_i = y_i - \bar{y}$.

Once the central coordinates and radius of the best fit circle are found, AUGUR masks the image so that only the portion of the image close to the limb is visible in the circle fit (Fig. 4), this allows for the image correlation to focus on certain lunar features in the image. We use a mask on the inner portion of the data to cancel out any effect the light gradient had on the lunar features, which would lead to a false correlation of the image later.

Computing a least-squares circle fit for the Sobel filter data allows for us to align the lunar limb in the image exactly with the projection of the Moon generated for each observation. Locating the lunar limb constrains the image

data to a certain part of the lunar surface, however the rotation of that image compared to the sub-observer latitude and longitude is unknown for each data set. Using the circle fit allows for us to correlate the image among different rotation angles by rotating it around that common central axis with the lunar projection.

Before comparing the image to the lunar projection, we first convert both the image and the projection into a binary feature map by using image thresholding. Using a pixel threshold brings out notable lunar features such as Grimaldi crater and Mare Crisium for AUGUR to focus on during the correlation. The thresholding limit assumes a darker pixel value corresponds to a more notable lunar features and patterns (such as the lunar Mare) and assigns those with a value of 1 in the binary map.

Once AUGUR converts both the impact image and the lunar projection into binary feature maps, it is then possible to measure the correlation at different rotation angles by overlaying the two binary images and counting the number of pixels that match in each. AUGUR counts the number of matched pixels for rotation angles between ± 30 degrees, with a 0 degree rotation angle starting at due East (0 degrees) for the Eastern hemisphere or due West (180 degrees) for the Western hemisphere. The positive direction for the rotation degree angles follows a counter-clockwise direction. Binary map comparisons for both hemispheres can be found in Fig. 5 with the correlation results in Fig. 6.

For the Eastern hemisphere of the Moon the rotation angle with the maximum number of pixels matched (highest correlation value) will be equivalent to the rotation angle of the final image. However, with the Western hemisphere, the maximum number of matched pixels is associated with an incorrect rotation angle due to Oceanus Procellarum acting as a false positive match. To combat this false match in rotation angle, AUGUR uses a third order polynomial fit to

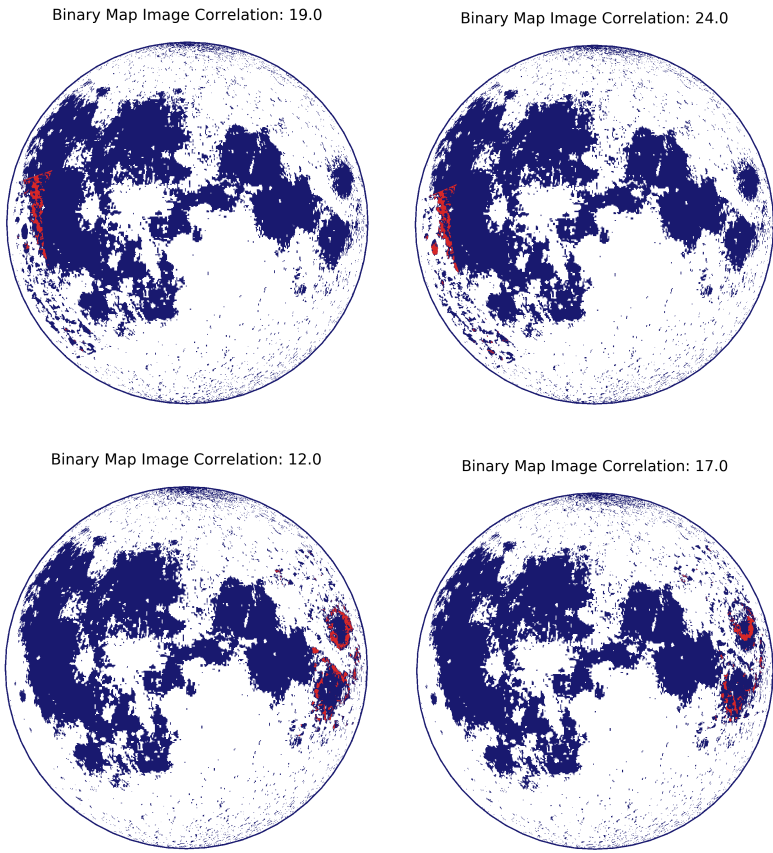


Figure 5: A binary version of the masked images in Fig. 4 is compared to the lunar projection threshold image. The white background corresponds to no features, the dark blue relates to a feature in one image but not in the other, and the red pixels represent a positive match between images. The top progression shows a typical correlation match for the Western hemisphere and the bottom shows one for the Eastern hemisphere. The number in each panel corresponds to the rotation degree of the image that is being tested. The central image shows the correlation at the correct degree (this was found to be 12 degrees for the Eastern image and 24 degrees for the Western). The surrounding images show examples of correlation matches for incorrect rotation degrees.

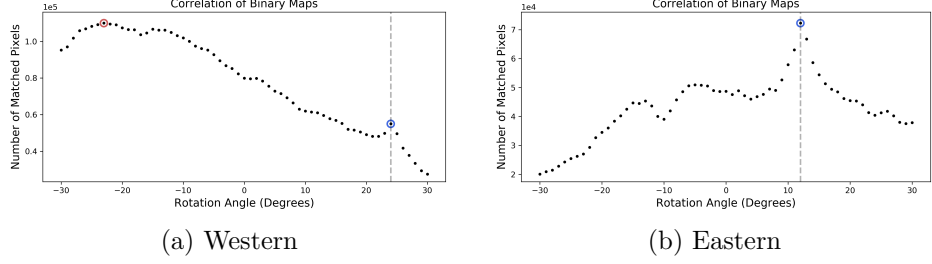


Figure 6: Results of the correlation between the two binary images for each hemisphere. The x-axis represents the rotation degree of the image and the y-axis corresponds to the number of pixels matched between the images at that degree. The blue circle and vertical dashed line indicates the correct rotation degree, where the red circle indicates a possible false rotation angle match. (a) The global maximum of the data does not correspond to the correct rotation angle and produces a false positive match, thus needs further analysis and (b) shows the same process for the Eastern hemisphere, however, the maximum matches with the correct rotation angle and does not need further analysis.

smooth the data and bring out local maxima that is associated with the correct rotation angle. This smoothed data and local maxima detection for the Western hemisphere correlation data is shown in Fig. 7.

After a rotation angle is obtained for the image, AUGUR can then complete the transformation of the coordinates from detector space (pixels) to selenographic coordinates (β, λ) using

$$\beta = \sin^{-1} \left(\cos(c) \sin(\beta_1) + \frac{y \sin(c) \cos(\beta_1)}{\rho} \right) \quad (5a)$$

for the latitude (β) and

$$\lambda = \lambda_0 + \tan^{-1} \left(\frac{x \sin(c)}{\rho \cos(\beta_1) \cos(c) - y \sin(\beta_1) \sin(c)} \right) \quad (5b)$$

for the longitude (λ). Where $\rho = \sqrt{x^2 + y^2}$ and $c = \sin^{-1}(\rho)$. Here (x, y) are the pixel coordinates of the LIF and (β_1, λ_0) are the sub-observer latitude and longitude previously obtained from *JPL Horizons* (Kopal, 1965).

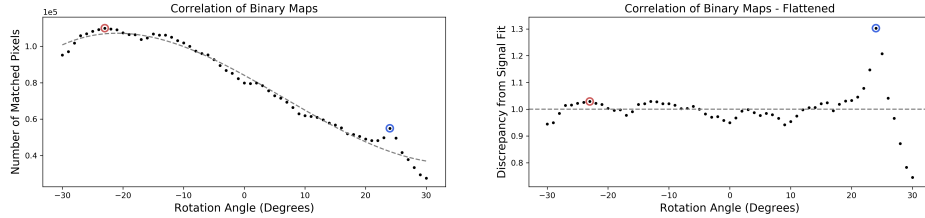


Figure 7: Extra analysis needed to achieve a correct rotation degree match by locating local maxima. The blue circle indicates the correct rotation degree, the red circle indicates a possible false rotation degree match, and the grey dashed line represents the best fit. a) Results of the correlation between the two binary images for the Western hemisphere with a best fit line. The x-axis represents the rotation degree of the image and the y-axis corresponds to the number of pixels matched between the images at the degree. b) The correlation data for the Western hemisphere that has been smoothed by dividing the data by its best fit to bring out the local maxima at 24 degrees. The x-axis represents the rotation degree of the image and the y-axis relates to the discrepancy from the best fit with a value of 1 being an exact match.

5. Source of impactors

The next step of the analysis is to identify the origin of the impactors, because it will provide information about their nature. In general, a meteoroid may originate from a meteoroid stream or from the background sporadic population of small near-Earth objects (NEOs). In the case of streams, the vast majority are of cometary origin and only a few are associated with asteroidal activity (e.g. Geminids). In order to estimate the kinetic energy (KE) of an impactor and subsequently its mass, it is essential to know the speed (v_{im}) at which it impacted onto the lunar surface and, if possible, the density of the object. The v_{im} is obtained by linking the impactor to its source, either a known meteoroid stream or the sporadic background population. To link the meteoroid that produced a flash to a meteoroid stream, we use the methods described in Avdellidou & Vaubaillon (2019) and in Madiedo et al. (2015b), after adjustments for the purposes of this work.

The first thing is to check whether the impact happened during an outburst of a meteoroid stream or not. Then, we compute the solar longitude difference between the time of the impact flash and that of the stream's maximum activity.

In this work we do not use the solar longitudes that are provided in the literature but we calculated them using established methods (Steyaert, 1991). If such difference is above a selected threshold the stream is omitted. Next, the difference of solar longitudes is converted into a difference of time which is used to correct the stream's radiant equatorial coordinates $(\text{Ra}, \text{Dec})_{ST}$ for the radiant drift. After that, the vector going from the centre of the Moon to the impact point is converted from Moon-centred coordinates into ICRS coordinates $(\text{Ra}, \text{Dec})_{imp}$ by taking into account the orientation of the Moon. Then the angular distance between the corrected stream radiant coordinate $(\text{Ra}, \text{Dec})_{ST}$ and $(\text{Ra}, \text{Dec})_{imp}$ are computed, and is checked if such distance is below a selected threshold and if not, the stream is eliminated. If a stream passes all these stages is considered as a candidate.

Once a meteoroid stream is a candidate, we compute the speed at which a meteoroid from the said stream will impact the lunar surface. Using SPICE, we obtain the ephemerides of the Moon at the time of impact and compute the heliocentric distance of the Moon. This is used to determine the relative distance between the Moon and the stream's nodes (ascending, descending). By checking which distance is the closest, we retrieve the true anomaly of the closest node, which is used to compute the mean anomaly M according to:

$$M = \nu - 2e \sin \nu + \left(\frac{3}{4}e^2 + \frac{1}{8}e^4 \right) \sin 2\nu - \frac{1}{3}e^3 \sin 3\nu + \frac{5}{32}e^4 \sin 4\nu + \dots \quad (6)$$

where ν is the true anomaly and e the eccentricity of the stream. The reason we need the stream's mean anomaly is to construct its SPICE orbital elements array which consist of the stream relative information: perifocal distance, eccentricity, inclination, longitude of the ascending node, argument of periapse, mean anomaly at epoch, epoch (the instant at which the state of the body is

specified by the elements) and the Sun gravitational parameter (since orbits are heliocentric, J2000). All these orbital elements, except for the mean anomaly, are provided by the IAU Meteor Data Center³. Using this array, we determine the epoch when the closest distance in the stream’s orbit to the Moon is reached. This epoch is used to compute the heliocentric distance of the stream’s meteoroids and compare it to that of the Moon in order to ensure that the difference is not bigger than 0.1 au. This criterion value is based on orbital mechanics consideration: the difference in velocity vector makes sense only if the stream and the Moon are approximately at the same heliocentric distance (see also Neslusan et al., 1998). Then we compute the difference between the velocity of the Moon at the epoch of the impact and that of the stream’s meteoroids at the epoch of the closest distance. The resulted relative speed is the final v_{im} .

Next we eliminate the candidate streams that are geometrically impossible to produce the studied impact. For a given stream the lunar sub-radiant point is the point on the lunar surface where the radiant of the stream is directly above (Cudnik, 2009). To compute the selenographic coordinates of the sub-radiant points, we first obtain the position of the Moon at the time of the impact in ECLIPJ2000. Next, using the stream’s SPICE array (constructed earlier), we search its closest approach to the Moon, retrieve its coordinates in ECLIPJ2000 and determine the stream’s position with respect to the centre of the Moon. The coordinates then are transformed to the Moon Principal Axes frame, which is a non-inertial body-fixed frame, where the z-axis is along the Moon’s rotation axis. At this point, we have the stream’s sub-radiant point $(x_{sub}, y_{sub}, z_{sub})$, and we compute the angular separation (θ) from the LIF location. This is done by converting the planetocentric latitude and longitude of the LIF to rectangular coordinates (x_f, y_f, z_f) and compute the angle between the two vectors (θ).

³<https://www.ta3.sk/IAUC22DB/MDC2007/>

Any meteoroid stream that has an angle between its sub-radiant point and an impact location larger than 90 deg is excluded.

At this stage we probabilistically determine the most likely parent meteoroid stream, or whether it comes from the sporadic background population, following the procedure that is described in Madiedo et al. (2015b). The probability of a stream being the source of a LIF is:

$$p^{ST} = \frac{N^{ST}}{N^{ST} + N^{OtherST} + N^{SPO}} \quad (7)$$

N^{ST} is the number of impacts per unit time that can be produced by a stream, $N^{OtherST}$ the number of impacts per unit time that can be produced by other active streams and N^{SPO} is the number of impacts per unit time produced by the sporadic population. As for the probability of an impact flash coming from the sporadic population, it will be:

$$p^{SPO} = 1 - \sum_i p^{ST_i} \quad (8)$$

where i represents the active streams that may be the source of the LIF. Following the assumptions of Madiedo et al. (2015b) (see paper for more details), the probability of a stream being the source of a LIF becomes:

$$p^{ST} = \frac{\sigma \nu^{ST} \gamma^{ST} \cos(\theta) ZHR_{Earth}^{ST}(peak) 10^{-b|\lambda - \lambda_{peak}|}}{\nu^{SPO} \gamma^{SPO} H R_{Earth}^{SPO} + \sigma \nu^{ST} \gamma^{ST} \cos(\theta) ZHR_{Earth}^{ST}(peak) 10^{-b|\lambda - \lambda_{peak}|} + \kappa} \quad (9)$$

with

$$\kappa = \sum_i \sigma \nu_i^{ST} \gamma_i^{ST} \cos(\theta_i) ZHR_{i,Earth}^{ST}(peak) 10^{-b_i |\lambda_i - \lambda_{i,peak}|} \quad (10)$$

where

- $\sigma = \frac{d_{Earth}}{d_{Moon}}$; d is the distance to the radiant of the stream.

- $\nu = \left(\frac{m_0 v_{im}^2}{2}\right)^{s-1} E_{min}^{1-s}$; v_{im} is the impact velocity, m_0 is the mass of a meteoroid stream producing on Earth a meteor of magnitude +6.5, s is the mass index, which is related to the population index r ($s = 1 + 2.5 \log r$) and $E_{min} = \eta E_{lum,min}$ is the minimum *KE* detectable from the Earth with η the luminous efficiency and $E_{lum,min}$ the minimum luminous energy detectable from the Earth. The selected values for η are described immediately after, in §6.
- $\gamma = \frac{\Phi_{Moon}}{\Phi_{Earth}}$, with $\Phi = 1 + \left(\frac{v_{esc}}{V}\right)^2$ as the gravitational focusing factor, v_{esc} as the escape velocity of the central body and v_{im} as the impact speed.
- θ is the angular distance between the sub-radiant point of the stream on the Moon and the location of the impact flash on the lunar surface.
- $ZHR_{Earth}^{ST}(peak)$ is the zenith hourly rate of the stream on Earth at its peak activity with λ_{peak} to be the solar longitude at such activity peak.
- λ is the solar longitude at the time of the LIF.
- b is the slope governing the behaviour of ZHR away from its peak (Jenniskens, 1994, for more details).
- HR_{Earth}^{SPO} is the average hourly rate of sporadic events.

In Eq. 9, the parameters $ZHR_{Earth}^{ST}(peak)$, λ_{peak} , b and r need to be specified for each potential stream where values are retrieved from the literature (Jenniskens, 1994, 2006; Moorhead et al., 2019), the International Meteor Organization (IMO)⁴ and the American Meteor Society (AMS)⁵. Despite our extensive search to get these parameters for every stream we found to be a potential source for an impact flash, we still miss values for the above parameters of some

⁴<https://www.imo.net/resources/calendar/>

⁵<https://www.amsmeteors.org/meteor-showers/2020-meteor-shower-list/>

minor streams. For those streams, we carried out actions based on the missing parameter. In the case of the population index r , we examined all the available values for all the streams and selected the most probable one to be 2.5. As for the adopted r value for the sporadic background, we selected it to be 3 (see Madiedo et al., 2015b, and reference therein). For b values, we followed the convention set by Jenniskens (1994). For minor streams that have high inclination ($i > 15$ deg), which turned out to be all of them in our case, the value of b can be set to 0.19. For HR_{Earth}^{SPO} we assigned 10 meteors h^{-1} (see Madiedo et al., 2015b, and reference therein). The m_0 is computed using the Eqs. (1) and (2) from Hughes (1987), $E_{lum,min}$ using the Eqs. (5) & (6) from Suggs et al. (2014), Eqs. (18) from Madiedo et al. (2015b) and the equations described in §6.1. The computation of $E_{lum,min}$ requires information about the systems used to observed each LIF such as the limiting magnitude and is obtained from the respective LIF publications. The results from the whole dataset, regarding the origin of an impactor and the respective probability are given in Tab. 4.

6. Physical properties: mass and size

In this work we have collected LIF datasets from different projects (see §2) and we unite them in one single dataset in order to construct the size distribution. To do so, each dataset requires a different treatment.

During an impact event the KE of the impactor is divided in several parts; one part is released as luminous energy, E_{lum} , and is detected by telescopes. This is used in order to derive the masses and later the sizes of the impacting meteoroids. The E_{lum} is a small fraction η of the KE and thus the impacting mass is given by:

$$m = \frac{2E_{lum}}{v_{im}^2 \eta} \quad (11)$$

where the luminous efficiency η has been estimated by several studies (Bellot

Rubio et al., 2000; Moser et al., 2011; Bouley et al., 2012).

6.1. NELIOTA

According to previous laboratory and observational studies, an impact flash is assumed to be a black body radiator and its spectral energy distribution is described by the Planck formula:

$$B(\lambda, T) = \frac{2hc}{\lambda^5} \frac{1}{\exp(\frac{hc}{\lambda k_B T}) - 1} \quad (12)$$

calculated in $\text{erg cm}^{-2}\text{s}^{-1}\text{A}^{-1}\text{sr}^{-1}$, where $h = 6.62 \times 10^{-27} \text{ g cm}^2\text{s}^{-1}$ is the Planck constant, $c = 3 \times 10^{10} \text{ cm s}^{-1}$ is the speed of light, $k_B = 1.38 \times 10^{-16} \text{ g cm}^2\text{s}^{-2}\text{K}^{-1}$ is the Boltzmann constant, T and λ are the temperature of the flash and the wavelength of the photons, respectively. In addition, we accept that the observed flux F for a given observing time where the Moon is at distance D from the observer, comes from a half black body-like sphere of radius r (in m) and thus is given by:

$$F = \frac{\pi r^2}{D^2} B(\lambda, T) \quad (13)$$

In this work we follow the same assumptions and methodology that are described in details by Avdellidou & Vaubaillon (2019) and here we remind the main steps. According to Xilouris et al. (2018) the NELIOTA magnitudes R and I are calibrated in the Cousins system and the $R - I$ colour is described by the the following equations:

$$\begin{aligned} R &= -2.5 \log\left(\frac{\pi r^2}{D^2}\right) - 2.5 \log(\xi_R) - 21.1 - ZP_R \\ I &= -2.5 \log\left(\frac{\pi r^2}{D^2}\right) - 2.5 \log(\xi_I) - 21.1 - ZP_I \end{aligned} \quad (14)$$

$$R - I = -2.5 \log\left(\frac{\xi_R}{\xi_I}\right) - (ZP_R - ZP_I) \quad (15)$$

where $ZP_R = 0.555$ and $ZP_I = 1.271$, as defined by Bessell et al. (1998). The parameters ξ are the spectral flux density of each band and are defined as:

$$\xi_R = \frac{\int B(\lambda, T) R c(\lambda) d\lambda}{\int R c(\lambda) d\lambda} \quad \xi_I = \frac{\int B(\lambda, T) I c(\lambda) d\lambda}{\int I c(\lambda) d\lambda} \quad (16)$$

where $R c(\lambda)$ and $I c(\lambda)$ are the responses of the Cousin filters. The theoretical curve that relates the $R - I$ colour with flash temperature for this observational setup has been already estimated and presented in Avdellidou & Vaubaillon (2019). For each flash, given the $R - I$ we obtain its T and we can evaluate the ξ_R and ξ_I . Evaluating Eqs. 14, we compute for each event the T of the LIF (Fig. 8) and the radius r of the theoretical area of emission. To estimate the error in T , a Monte Carlo approach is adopted with typically 10^5 iterations. At each iteration, a temperature value is derived from a new set of R and I that are extracted from Gaussian distributions centred on the nominal R and I values of the LIF and standard deviations equal to the magnitude errors given by NELIOTA and/or literature (Liakos et al., 2020). It has been stated that the NELIOTA R and I magnitude values and errors, as presented in the web-page, are an approximation and therefore when possible we use the published ones (Xilouris et al., 2018; Liakos et al., 2020).

Knowing now the temperatures and radii of the luminous events we can calculate the E_{lum} from:

$$E_{lum} = Lt \quad (17)$$

where t the duration of the luminous event, L the luminosity that is given by:

$$L = \pi^2 r^2 \int_{400}^{900} B(\lambda, T) d\lambda \quad (18)$$

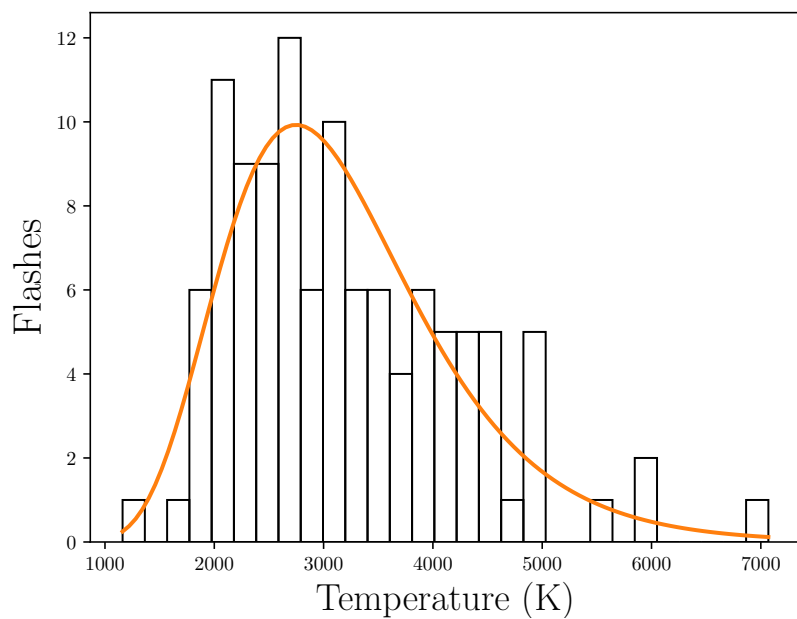


Figure 8: Temperature distribution of the observed flashes. The values correspond to the peak temperature measured from the initial R and I frames of each flash.

and finally we evaluate Eq.11. For the impact flashes that are detected in both cameras in at least two frames we derive the R and I magnitudes (see Tab. 1) for all frames using the Source Extractor tool (Bertin & Arnouts, 1996) as described in detail in Avdellidou & Vaubaillon (2019). For each of those frames the E_{lum} is calculated and summed in order to evaluate the Eqs. 17&18. Table 3 contains the derived T and E_{lum} for the NELIOTA data.

For the impacts that are associated with meteoroid streams we use the v_{im} as estimated before, whereas for impacts that come from the background population we assume a velocity of 24 km s^{-1} (McNamara et al., 2004). The η values were selected to be $\eta_1=1.5 \times 10^{-3}$ and $\eta_2=5 \times 10^{-4}$ (Bouley et al., 2012) and thus two mass datasets are produced (Tab. 4). Here we have to clarify that the same η values were used to evaluate Eq. 9 and make the link to either the background population or a meteor stream.

6.2. Marshall Space Flight Center

The analysis of the data from the Marshall Space Flight Center is simpler. As described before, the input data for this work are the LIFs presented in Suggs et al. (2014). We evaluate Eq. 11 using the peak E_{lum} that is presented in their Table 1 (and we repeat in Tab. 3) and the v_{im} we derived by re-estimating the origin (meteor stream or background) of each of their flashes (see §5). The final masses for this dataset were derived by using the η_S expression as described in (Suggs et al., 2014) and given by the Eq. (8) of that study. In addition, masses and sizes were derived using the η_1 and η_2 values for comparison purposes. The same η were also used to evaluate Eq. 9 for Marshall Space Flight Center dataset (Tab. 4).

6.3. Other observations

For the rest of the datasets presented in §2 we follow two paths. For the events that have published E_{lum} we use directly these values (Ait Moulay Larbi

Table 1: Multi-frame events. Magnitudes of the initial frames were taken from the literature or NELIOTA website, while the rest were calculated as described in Avdellidou & Vaubaillon (2019). T is estimated as described in §6.1.

Flash ID/ frame	$R \pm \sigma_R$ (mag)	$I \pm \sigma_I$ (mag)	$T \pm \sigma_T$ (K)
2/a	6.67 ± 0.07	6.07 ± 0.06	4429 ± 326
2/b	10.01 ± 0.17	8.26 ± 0.07	1941 ± 203
13/a	8.27 ± 0.04	6.32 ± 0.01	1803 ± 14
13/b	9.43 ± 0.12	7.44 ± 0.02	1736 ± 87
19/a	9.17 ± 0.07	8.07 ± 0.03	2991 ± 149
19/b	13.00 ± 1.50	8.96 ± 0.08	2228 ± 1141
20/a	8.52 ± 0.03	7.04 ± 0.01	2261 ± 44
20/b	10.01 ± 0.14	8.27 ± 0.07	1944 ± 176
20/c	11.32 ± 0.25	9.14 ± 0.08	1634 ± 174
40/a	9.16 ± 0.09	7.73 ± 0.02	2333 ± 139
40/b	11.19 ± 0.53	9.68 ± 0.11	2433 ± 963
42/a	8.78 ± 0.05	7.74 ± 0.02	3019 ± 108
42/b	11.78 ± 1.52	8.85 ± 0.05	2583 ± 1492
47/a	8.36 ± 0.04	7.30 ± 0.02	3089 ± 116
47/b	11.02 ± 0.30	8.81 ± 0.03	1667 ± 194
51/a	8.50 ± 0.11	7.16 ± 0.02	2653 ± 134
51/b	7.84 ± 0.07	6.60 ± 0.02	2654 ± 133
51/c	8.98 ± 0.14	7.45 ± 0.03	2205 ± 197
51/d	10.02 ± 0.25	8.21 ± 0.04	1907 ± 250
62/a	10.12 ± 0.20	9.29 ± 0.10	3721 ± 724
62/b	10.9 ± 0.30	9.02 ± 0.10	1862 ± 298
65/a	6.65 ± 0.10	5.49 ± 0.06	2784 ± 241
65/b	8.06 ± 0.23	6.68 ± 0.07	2424 ± 378
69/a	9.64 ± 0.16	8.21 ± 0.07	2312 ± 250
69/b	10.13 ± 0.30	8.21 ± 0.70	2363 ± 928
71/a	8.95 ± 0.13	8.02 ± 0.07	3371 ± 438
71/b	10.94 ± 0.40	9.11 ± 0.09	1964 ± 426
94/a	8.40 ± 0.10	5.6 ± 0.01	1161 ± 40
94/b	12.7 ± 1.10	8.34 ± 0.04	843 ± 335

et al., 2015), while for the rest we estimate the E_{lum} using the method described in Madiedo et al. (2015b). The E_{lum} values that we adopted or derived are presented in Tab. 3. Again we use η_1 and η_2 values, while the v_{im} for each flash is derived again in §5 with the same method as for the other datasets (Tab. 4).

6.4. Size frequency distribution of lunar impactors.

The masses are converted to sizes assuming spherical-shaped meteoroids and using density estimations from the literature (Babadzhanov & Kokhirova, 2009). For the events that are linked to eta Aquarids (ETA) we assign the same density that is estimated for Orionids $\delta=0.9 \text{ gr cm}^{-3}$ since both streams originate from comet Halley. For the meteoroids that originate from the background population or from sources that have no density estimations we assume $\delta=1.8 \text{ gr cm}^{-3}$ (Avdellidou & Vaubaillon, 2019). Finally we group the diameters of all the 307 impactors (see Tab. 4) and construct a global size frequency distribution (SFD) (Fig. 9).

7. First LIF detection from Observatoire de la Côte d’Azur, Nice, France

In order to test the aforementioned detection and analysis methods we performed observations during May 2020. The telescope used was a MEADE ACF 40 cm equipped with a CMOS ASI ZWO 183 mono camera. The telescope was guiding on the lunar crescent using the lunar autoguider that our team developed specifically for this project. The frame rate was 20 fps and the integration time was 0.05 seconds. On the night of May 27th, 2020 at 20:48:49.420 UTC, we detected our first impact flash (see Fig. 10) from the Observatoire de la Côte d’Azur and the site of Mt. Gros in Nice. This is the first live impact observed for the project “Flash!”, the first from the Observatoire de la Côte d’Azur and the first in France. Our algorithm that is described in §3 detected a luminous

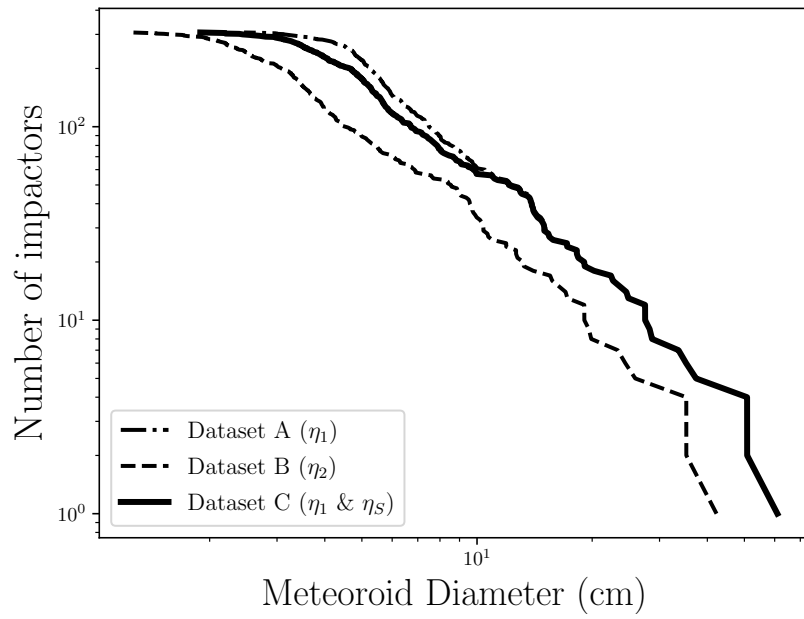


Figure 9: Dataset A contains meteoroid diameters form all detection that were analysed using $\eta_1 = 5 \times 10^{-4}$ and Dataset B diameters that were analysed using $\eta_2 = 1.5 \times 10^{-3}$. Dataset C is made of diameters that were produced using η_1 for NELIOTA and other minor observations, while data from Suggs et al. (2014) were analysed using their own η_S estimation.

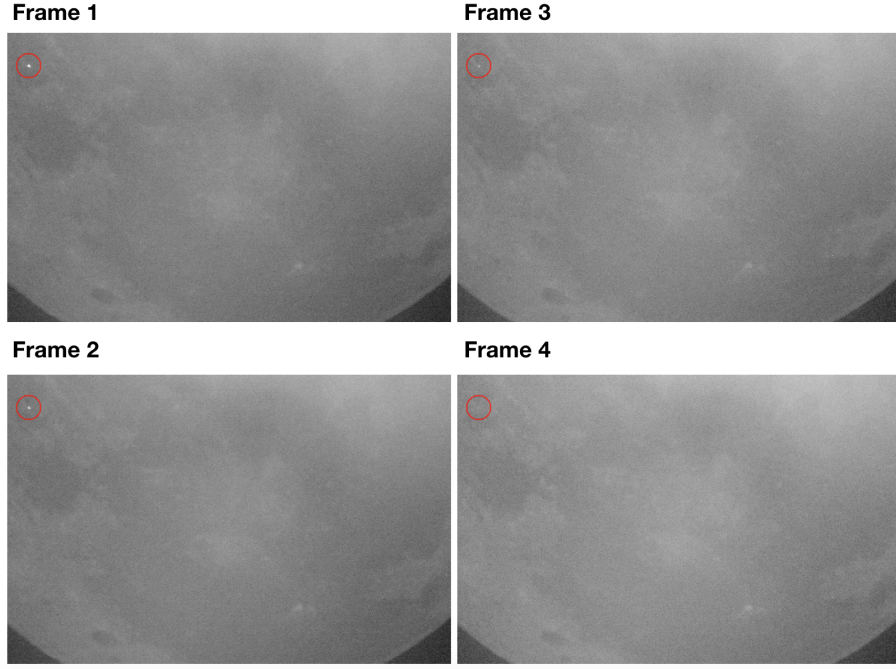


Figure 10: The evolution of the first lunar impact flash detected from France. The detection took place on the night of May 27th, 2020 at 20:48:49.420 UTC from OCA, Mt. Gros site.

event that lasted for four frames and thus has a duration of at least 0.2 seconds. According to our method described in §4 we estimate the impact coordinates to be: $\beta=-36.3\pm1$ and $\lambda=-25.4\pm1$. Although during the testing phase we performed observations only with one camera, we are confident that the luminous event that we detected is due to a LIF. Supporting factors is the long duration and the constant coordinates in all the frames. Following the procedure described in §5 we conclude that the meteoroid originated from the sporadic population.

8. Discussion

Comparing the new temperature distribution that we derive in this work, using 112 NELIOTA LIFs, with the previous one of Avdellidou & Vaubaillon

(2019) we see that the maximum T derived ($\sim 7,000$ K) is significantly higher. The updated data follow a log-normal distribution with mode $\sim 2,750$ K. The updated mode is slightly higher than the 2,550 K that was presented in Avdellidou & Vaubaillon (2019) and essentially the same with the theoretical estimation of 2,800 K (Nemtchinov et al., 1998). However, this difference with the previous analysis may not be statistically significant. The vast majority of the flashes appear to have a $T < 5,000$ K and only four events exceed this value. However, the discrepancy between the theoretical maximum T (3,776 K, Cintala, 1992) and the observed LIF T still remains. According to early laboratory experiments (Eichhorn, 1975, 1976) the impactors density may affect the flash temperatures but from the current dataset we do not observe a preference of impactors from a specific stream (and thus a specific composition and density) to produce those high T .

Regarding the mass estimation of the impactors there is a number of reasons that may affect the estimated values and subsequently the final slope of the SFD. First of all the measured E_{lum} may be underestimated. For example, for some frames luminosity can be below the background so it cannot be detected. Another reason, applied to NELIOTA data, is due to the fact that we take into account only the frames where the flash is detected in both cameras. All LIFs - even the single-frame ones - are detected in at least one more frame, usually in the I filter. Unfortunately, since the detection is not confirmed in the respective R filter frame we do not use it for the E_{lum} calculation, making the total E_{lum} of the flashes to be definitely underestimated. One could imagine that if we know the cooling rates we can correct the energy. However, the cooling rate is not the same for every LIF (Avdellidou & Vaubaillon, 2019), meaning that the E_{lum} ratio between the frames in the multiframe events is not constant. This prevents us from making assumptions for the lost energy.

Table 2: The change in impactor’s origin due to the different assumption for the luminous efficiency η (ID 6, 11, 18, 73 and 74) and due to differences in selenographic coordinate estimation (ID 17 and 18). NC is the nominal NELIOTA coordinates as described in §2, UC the updated ones as derived in this work, $\eta_1 = 5 \times 10^{-4}$ and $\eta_2 = 1.5 \times 10^{-3}$. The results for the total dataset are presented in Tab. A.6.

ID	NC	NC	UC	UC
	η_1	η_2	η_1	η_2
6	ETA	SPO	ETA	SPO
11	PER	SDA	PER	SDA
17	SPO	SPO	NIA	SPO
18	NIA	SPO	SPO	SPO
73	CAP	SPO	CAP	SPO
74	CAP	SPO	CAP	SPO

The most important factor that can change the mass estimation, even by an order of magnitude, is the luminous efficiency η . What η may also affect is the link to stream (or not) as it is a factor on which Eq. 9 depends. To understand if this dependence is significant we compare the probability results from both calculations. As it is seen in Tab. 2 by changing the luminous efficiency the link changes only for 5 LIFs out of 112 which we recon is not significant and thus may not affect the final SFD.

The link of an impactor to a specific meteoroid stream or to the sporadic population affects also the mass estimation as the speed alters significantly and may vary between 17 and 70 km/s! In this work we advanced from Suggs et al. (2014) by checking the full database of meteoroid streams and not only the strongest ones and we also advanced from Avdellidou & Vaubaillon (2019) as we investigate also the probability of the impactor to originate from the background population. Since we have two datasets of selenographic coordinates (Tab. A.5) one obtained from the literature and the other produced in this work, at least for the NELIOTA data, we compute the probabilities for both datasets (Tab. A.6). In principle any change in selenographic coordinates may place a LIF inside or outside of the lunar area on which a given meteoroid stream can impact. As it is seen in Tab. 2, by changing the selection of the selenographic coordinates

the link changes only for two out of 112 LIFs. This is an insignificant fraction that will not affect the global SFD of lunar impactors. The source probability for each impactor may be affected by the selection of the parameters b , r and m (for Eq. 9) that characterise each stream and are not always precisely known for each one. The most important uncertainty is introduced by the impact speed which is required in order to derive the meteoroid's mass. In the case where an impactor is linked to a meteoroid stream this problem is lifted. However, in the most numerous cases where the impactors are linked to the background population an average speed value is selected to be applied to all the events. Several average values have been adopted so far from the different LIF studies, ranging from 17 to 24 km s⁻¹ (Ortiz et al., 1999, 2000, 2006; Suggs et al., 2014; Madiedo et al., 2014). According to the impact speed distribution on the lunar surface by Le Feuvre & Wieczorek (2011) a minimum value can be as low as \sim 5 km s⁻¹ while the tail of the distribution can reach \sim 40 km s⁻¹. The distribution of the impacting speeds derived by McNamara et al. (2004) agrees with the low limit of Le Feuvre & Wieczorek (2011) but at the high end there is a longer tail where speeds can reach up to 65 km s⁻¹, with the average value being \sim 24 km s⁻¹. Therefore, in reality a meteoroid's speed can deviate from this average, resulting in masses up to 25 times larger or down to nine times smaller than the ones presented in this work, affecting the SFD.

Since the selection of η affects the final SFD we need to be careful on the way we link the data from the different sources. As it is seen in Fig. 9 the SFD slope in the very small impactor sizes is slightly affected if we do not use the η estimation of Suggs et al. (2014). Therefore, in order to be consistent with their study and results we adopt the Dataset C which uses the Marshall Space Flight Centre data processed with the η estimation for their own observing system, while for the rest we use the η values taken from the literature.

Halliday et al. (1996), using the fireball data from the Canadian camera network, derived an SFD of small impactors, breaking around the size of 10–15 cm in two segments with different slopes, those being \sim 1.3 for the smaller and \sim 3 for the larger objects. The SFD (Dataset 3 of Fig. 9) that we derive here appears also to have a small knee at the same sizes and corresponding slopes -1.4 and -2.2 respectively, while the vast majority of the meteoroids (80%) appear to have sizes < 10 cm.

9. Conclusions

In this work we present all the computational steps to (i) detect the lunar flashes that correspond to meteoroid impact events; (ii) identify their selenographic impact coordinates, that will later serve in the detection of the impact craters; (iii) to link an impactor to a meteoroid stream or to the background sporadic population; (iv) estimate their masses and sizes. We tested the previous steps to a suite of LIF events presented in the literature in the last 20 years. By unifying different datasets from various observers, requiring different approach in their analysis due to different observing methods, we constructed the lunar impactors' SFD of small sizes (cm-dm). Furthermore we applied the steps above in our own observations during the testing phase of our observing project with a result the detection of the first LIF for the Observatoire de la Côte d'Azur.

Acknowledgements

This work was supported by the Programme National de Planétologie (PNP) of CNRS/INSU, co-funded by CNES and by the program “Flash!” supported by Crédits Scientifiques Incitatifs (CSI) of the Université Nice Sophia Antipolis. CA was supported by the French National Research Agency under the project

“Investissements d’Avenir” UCA^{JEDI} with the reference number ANR-15-IDEX-01. Part of this work was also supported by the Planetary Astronomy program of the National Aeronautics and Space Administration, as well as NASA’s Lunar Reconnaissance Orbiter project. We would like to thank E. Bondoux for helping to access the telescope facility at Observatoire de la Côte d’Azur.

Table 3: The total dataset that is used in this work. References are: Flash ID 1-112 from NELIOTA website; 182-307 from Suggs et al. (2014); 113, 114, 116, 120 from Dunham et al. (2000); 115, 118, 119, 120, 122 from Ortiz et al. (2000); 126-129 from Ortiz et al. (2002); 132-134 from Ortiz et al. (2006); 136-139, 144, 171-177 from Ortiz et al. (2015); 117, 130, 131 from Cudnik et al. (2003); 123-125 from Yanagisawa & Kisaichi (2002); 135 from Yanagisawa et al. (2006); 151, 159-170 from Madiedo et al. (2015b); 140-143, 145-150 from Madiedo et al. (2015a); 154-158 from Madiedo et al. (2016); 180 from Madiedo et al. (2018); 152, 153, 178, 179, 181 from Ait Moulay Larbi et al. (2015).

ID	Date-Time (UT)	T (K)	E_{lum} (J)	ID	Date-Time (UT)	T (K)	E_{lum} (J)
1	20170201-17:13:57.863	2969 ± 276	14743	155	20130417-21:38:02.000		254186
2	20170301-17:08:46.573	4429 ± 326	334934	156	20130417-22:12:25.000		254186
3	20170301-17:13:17.360	3446 ± 367	34803	157	20130417-22:39:00.000		87927
4	20170304-20:51:31.853	4168 ± 714	27887	158	20130418-22:25:50.000		363078
5	20170401-19:45:51.650	2148 ± 178	17069	159	20130811-20:16:33.000		405394
6	20170501-20:30:58.137	2474 ± 310	17844	160	20130811-20:43:19.000		80695
7	20170627-18:58:26.680	1929 ± 340	17107	161	20130811-21:08:14.000		534413
8	20170628-18:45:25.803	3134 ± 1050	41286	162	20130812-19:49:57.000		1580881
9	20170719-02:00:36.453	1894 ± 387	18089	163	20130812-20:08:29.000		690079
10	20170728-18:21:44.850	1823 ± 305	16586	164	20130812-20:14:55.000		2084006
11	20170728-18:42:58.027	3040 ± 716	17061	165	20130813-20:18:29.000		70542
12	20170728-18:51:41.683	3143 ± 732	13978	166	20130813-20:39:01.000		64336
13	20170728-19:17:18.307	1803 ± 14	168021	167	20130813-21:08:52.000		6158582
14	20170816-01:05:46.763	4654 ± 969	17359	168	20130813-21:12:47.000		134416
15	20170816-02:15:58.813	2142 ± 374	18856	169	20130813-21:14:53.000		70542
16	20170816-02:41:15.113	1993 ± 347	19372	170	20130813-22:03:48.000		976070
17	20170818-02:02:21.417	1970 ± 209	11077	171	20131205-18:29:41.000		353172
18	20170818-02:03:08.317	2447 ± 212	14897	172	20131205-19:00:06.000		185347
19	20170914-03:17:49.737	2991 ± 149	124745	173	20131205-19:03:14.000		613742
20	20170916-02:26:24.933	2261 ± 44	101651	174	20131206-18:56:13.000		225738
21	20171013-01:54:21.710	3463 ± 315	30309	175	20131207-19:31:06.000		916241
22	20171013-02:33:43.560	5871 ± 1654	18560	176	20131226-18:42:15.000		404864
23	20171016-02:46:45.613	2590 ± 314	10460	177	20131226-20:52:02.000		845880

Table 3 : Continued from previous page.

24	20171026-17:59:42.880	4459 ± 1326	26725	178	20141126 -19:12:02.900	350000
25	20171114-03:34:15.203	3276 ± 483	16235	179	20141225 -18:08:43.620	45000
26	20171123-16:17:33.000	6039 ± 1609	17702	180	20150325 -21:00:16.800	823607
27	20171212-02:48:08.410	2115 ± 318	22917	181	20151117 -19:26:37.290	63000
28	20171212-04:30:00.623	4260 ± 1331	23804	182	20060916 -09:52:54.000	21400
29	20171213-04:26:57.717	4891 ± 1430	19272	183	20060928 -00:42:57.000	31400
30	20171214-04:35:09.967	2763 ± 104	115919	184	20061029 -01:18:43.000	49800
31	20180112-03:54:03.027	4080 ± 580	19275	185	20061117-10:46:26.000	15600
32	20180323-17:24:19.240	2538 ± 478	30299	186	20061117-10:56:33.000	85800
33	20180410-03:36:57.767	3838 ± 468	52794	187	20061117-11:02:29.000	51700
34	20180609-02:29:18.467	3436 ± 804	28259	188	20061117-11:09:10.000	19300
35	20180619-19:12:09.650	3672 ± 838	25623	189	20061124-23:58:12.000	41100
36	20180619-20:00:48.490	4420 ± 1320	26396	190	20061125-00:55:54.000	37800
37	20180619-20:04:09.773	2400 ± 938	99586	191	20061126-00:59:16.000	56700
38	20180709-01:44:19.410	3021 ± 777	12251	192	20061126-01:28:43.000	17800
39	20180806-01:57:43.687	2175 ± 211	29217	193	20061126-01:30:29.000	18600
40	20180806-02:38:14.303	2337 ± 139	83084	194	20061214-08:46:02.000	10700
41	20180807-01:33:54.757	2270 ± 391	14709	195	20061214-08:50:35.000	28400
42	20180807-01:35:45.167	3019 ± 108	228979	196	20061214-08:51:20.000	16200
43	20180807-02:33:18.183	4563 ± 797	16705	197	20061214-08:56:42.000	23000
44	20180807-03:10:33.303	4921 ± 1713	26616	198	20061214-09:00:21.000	23400
45	20180808-02:19:55.007	2685 ± 591	11041	199	20061214-09:03:32.000	5830
46	20180808-02:28:23.407	4378 ± 1011	7945	200	20061215-09:15:14.000	22200
47	20180808-02:29:44.573	3089 ± 116	78083	201	20061215-09:17:39.000	60500
48	20180808-02:52:25.877	2578 ± 629	14905	202	20070223-00:47:45.000	36100
49	20180815-18:08:16.637	1665 ± 245	10300	203	20070223-04:02:44.000	13200
50	20180904-01:33:52.977	4210 ± 1401	32155	204	20070422-01:15:05.000	9950
51	20180905-01:51:37.400	2653 ± 134	304193	205	20070422-01:15:41.000	10200
52	20180905-02:47:54.403	2263 ± 565	30205	206	20070422-01:38:31.000	49400

Table 3 : Continued from previous page.

53	20180906-02:00:33.053	4423 ± 1357	10596	207	20070422-03:12:21.000	111000
54	20180906-03:10:04.087	2520 ± 464	9449	208	20070422-03:52:37.000	20600
55	20181015-18:17:49.313	4014 ± 837	34563	209	20070422-04:22:27.000	29500
56	20190209-17:29:38.337	5541 ± 1567	20380	210	20070423-01:15:55.000	26400
57	20190209-18:17:00.010	4884 ± 1310	21083	211	20070423-02:23:21.000	16100
58	20190410-19:53:21.200	3625 ± 949	56442	212	20070423-03:01:10.000	19700
59	20190608-19:14:58.557	2403 ± 671	50255	213	20070423-04:08:49.000	33200
60	20190608-19:26:58.337	2760 ± 422	44120	214	20070423-04:38:22.000	20600
61	20190628-01:56:47.677	2550 ± 227	54849	215	20070423-04:40:46.000	10200
62	20190628-02:18:22.900	3721 ± 724	40805	216	20070423-04:42:35.000	84300
63	20190706-19:12:55.227	3314 ± 739	24127	217	20070423-04:59:58.000	46300
64	20190707-18:32:55.697	2621 ± 791	24500	218	20070521-02:50:53.000	40000
65	20190707-18:40:21.203	2786 ± 241	499475	219	20070521-03:10:07.000	13400
66	20190707-18:48:48.083	1895 ± 537	17730	220	20070809-09:10:50.000	64500
67	20190708-19:11:44.450	2133 ± 289	34823	221	20071006-08:42:52.000	20200
68	20190726-00:18:27.627	3100 ± 1036	33159	222	20071116-00:11:21.000	14400
69	20190726-00:41:35.187	2312 ± 250	153322	223	20071116-00:27:09.000	81200
70	20190727-01:13:12.237	2786 ± 807	30599	224	20080103-10:25:42.000	12000
71	20190727-01:17:49.790	3371 ± 438	73606	225	20080104-10:58:26.000	29200
72	20190727-02:12:25.050	3191 ± 516	28780	226	20080104-11:42:39.000	75400
73	20190727-02:37:22.717	4268 ± 859	18169	227	20080104-11:48:36.000	26600
74	20190727-02:59:56.457	2656 ± 395	36654	228	20080114-00:22:26.000	7480
75	20190727-03:01:26.127	2340 ± 217	57711	229	20080211-01:09:27.000	28900
76	20190728-01:33:40.120	2835 ± 431	20438	230	20080212-00:24:44.000	20200
77	20190728-01:59:21.347	2861 ± 835	23197	231	20080312-00:40:42.000	103000
78	20190728-02:00:53.887	3738 ± 1208	14775	232	20080312-01:13:31.000	12000
79	20190728-02:24:26.087	2964 ± 777	13729	233	20080312-02:03:07.000	10500
80	20190806-18:19:16.023	2039 ± 364	29172	234	20080313-01:38:48.000	3680
81	20190806-18:56:36.990	3228 ± 292	70373	235	20080313-02:04:22.000	45900

Table 3 : Continued from previous page.

82	20190806-18:59:15.737	7069 ± 1275	33357	236	20080409-02:16:38.000	202000
83	20190826-02:50:56.347	2101 ± 278	15024	237	20080410-01:15:25.000	23400
84	20190828-03:03:30.930	2768 ± 719	14219	238	20080607-02:27:23.000	125000
85	20190905-18:11:59.277	4551 ± 926	18714	239	20080607-03:31:31.000	36100
86	20190905-18:51:32.997	3882 ± 1042	25418	240	20080627-09:31:25.000	18400
87	20190923-03:36:21.557	3892 ± 1047	25990	241	20080728-08:35:37.000	4800
88	20190925-03:40:11.073	3215 ± 297	67009	242	20080728-08:47:07.000	16100
89	20191022-04:11:36.270	4161 ± 857	20050	243	20080728-09:05:16.000	22200
90	20191024-02:30:16.187	2106 ± 141	30447	244	20080729-09:43:11.000	39600
91	20191102-17:19:19.667	3554 ± 1052	31935	245	20080923-10:14:33.000	14600
92	20191103-17:49:38.487	3954 ± 969	41156	246	20080924-08:46:41.000	158000
93	20191201-16:14:30.210	4232 ± 620	41489	247	20081022-07:25:10.000	34500
94	20191201-16:23:13.797	1161 ± 40	30767557	248	20081022-07:51:31.000	22600
95	20191201-16:30:43.410	1992 ± 254	16556	249	20081022-10:03:14.000	14000
96	20191201-17:14:41.437	2001 ± 463	23623	250	20081022-10:30:21.000	14400
97	20191220-4:34:16.680	3269 ± 692	39684	251	20081102-23:48:40.000	15800
98	20200130-17:18:08.540	2251 ± 478	19939	252	20081103-00:11:06.000	43800
99	20200130-17:35:38.893	3980 ± 904	16695	253	20081103-23:59:24.000	14500
100	20200301-16:54:24.090	3015 ± 242	89794	254	20081104-00:04:06.000	22000
101	20200301-17:10:06.377	4857 ± 1686	27352	255	20081104-01:10:01.000	21600
102	20200327-17:40:25.320	2541 ± 181	20042	256	20081104-01:39:04.000	56200
103	20200329-18:14:10.877	2972 ± 576	13540	257	20081105-00:38:38.000	53200
104	20200329-19:16:46.510	3512 ± 672	20739	258	20081105-00:53:58.000	13700
105	20200428-19:19:54.527	3454 ± 371	43563	259	20081105-02:05:08.000	74800
106	20200625-18:28:18.340	2719 ± 204	114975	260	20081105-02:09:45.000	9410
107	20200626-19:52:31.570	2238 ± 154	25089	261	20081105-02:32:47.000	35800
108	20200726-19:08:21.287	3002 ± 315	14623	262	20081120-11:03:06.000	17900
109	20200726-19:10:25.427	2371 ± 100	34376	263	20081122-09:41:24.000	41100
110	20200813-00:57:10.703	2746 ± 456	22224	264	20081123-10:48:24.000	17400

Table 3 : Continued from previous page.

111	20200814-00:54:21.133	3831 ± 520	35614	265	20081123-11:15:53.000	12500
112	20200814-01:15:36.277	4839 ± 1087	19574	266	20081203-00:30:58.000	5080
113	19991118-03:05:44.890		2826860	267	20081203-02:09:04.000	36800
114	19991118-03:49:40.380		17836283	268	20090201-01:40:26.000	9670
115	19991118-03:49:40.380		17811259	269	20090201-02:04:46.000	14900
116	19991118-04:08:04.100		2826860	270	20090202-02:45:43.000	16200
117	19991118-04:12:27.830		1781126	271	20090303-02:51:43.000	10900
118	19991118-04:32:50.790		7090790	272	20090303-04:02:49.000	17900
119	19991118-04:34:49.520		447399	273	20090303-04:27:49.000	34800
120	19991118-04:46:15.520		17811259	274	20090330-01:43:11.000	25000
121	19991118-05:14:12.920		1123814	275	20090530-03:52:11.000	106000
122	19991118-05:15:20.220		2822894	276	20090619-09:00:07.000	56700
123	19991118-11:07:46.200		1147513	277	20090626-02:04:07.000	48900
124	19991118-11:18:05.900		456833	278	20091024-23:57:36.000	17900
125	19991118-12:11:45.500		456833	279	20091025-00:14:24.000	3890
126	20011118-18:10:36.000		711779	280	20091025-01:20:00.000	15900
127	20011118-18:12:21.000		492431	281	20091025-01:52:04.000	8900
128	20011118-18:19:55.000		373547	282	20091025-01:55:07.000	19300
129	20011118-18:27:46.000		5920318	283	20091025-01:58:10.000	33500
130	20011118-23:19:15.210		823711	284	20091025-02:37:58.000	17800
131	20011119-00:18:58.200		3063690	285	20091025-02:38:08.000	21600
132	20020219-19:40:04.000		688974	286	20091025-02:53:59.000	34800
133	20030205-19:24:43.000		355941	287	20091112-10:10:23.000	23400
134	20031226-17:36:38.000		948617	288	20091113-10:15:45.000	37800
135	20040811-18:28:26.900		51206	289	20091210-09:41:54.000	22400
136	20071214-19:18:06.000		74433	290	20091221-00:12:38.000	47600
137	20071214-19:28:48.000		373935	291	20091221-00:33:46.000	20800
138	20071214-19:50:57.000		67884	292	20100219-00:45:39.000	15600
139	20071214-20:42:57.000		939283	293	20100219-01:15:11.000	24100

Table 3 : Continued from previous page.

140	20110409-20:38:08.000	454006	294	20100421-02:48:03.000	14900
141	20110409-20:52:44.000	286458	295	20100518-01:38:31.000	14000
142	20110411-00:05:06.000	358438	296	20100518-01:56:33.000	7070
143	20111230-21:00:30.000	295838	297	20100518-02:31:10.000	52200
144	20111230-21:00:30.000	295838	298	20100708-08:48:56.000	508000
145	20120226-21:40:10.000	232379	299	20100902-06:54:16.000	25000
146	20120228-23:05:16.000	443568	300	20101004-09:27:01.000	29200
147	20120327-20:47:16.000	93003	301	20110109-01:17:55.000	23900
148	20120726-21:35:04.000	214427	302	20110226-09:39:29.000	14800
149	20121020-20:05:03.000	403696	303	20110226-10:38:26.000	15200
150	20121020-20:48:28.000	232303	304	20110408-01:32:18.000	61600
151	20120813 -03:55:08.000	393885	305	20110510-03:40:20.000	156000
152	20130206 -06:29:56.750	82000	306	20110823-07:39:07.000	15500
153	20130414-20:00:45.430	430000	307	20110823-09:58:32.000	12500
154	20130416-20:35:41.000	88427			

Table 4: Summary of the characteristics of the impactors. The meteoroid source (S) with its probability (P), its impact speed (v_{imp}) in km s^{-1} , mass (m) in gr and size (d) in cm are calculated using three different estimations for the luminous efficiency η . We use $\eta_1 = 5 \times 10^{-4}$ ($S_1, P_1, v_{imp1}, m_1, d_1$) and $\eta_2 = 1.5 \times 10^{-3}$ ($S_2, P_2, v_{imp2}, m_2, d_2$) for the whole dataset. Additionally, for the data taken from Suggs et al. (2014) we use the expression of η_S that is described in their work ($S_S, P_S, v_{impS}, m_S, d_S$).

ID	S_1	P_1	v_{imp1}	m_1	d_1	S_2	P_2	v_{imp2}	m_2	d_2	S_S	P_S	v_{impS}	m_S	d_S
1	SPO	0.79	24.00	102.38	4.77	SPO	0.82	24.00	34.13	3.31					
2	SPO	0.99	24.00	2325.93	13.51	SPO	1.00	24.00	775.31	9.37					
3	SPO	1.00	24.00	241.69	6.35	SPO	1.00	24.00	80.56	4.41					
4	SPO	0.99	24.00	193.66	5.90	SPO	0.99	24.00	64.55	4.09					
5	SPO	1.00	24.00	118.53	5.01	SPO	1.00	24.00	39.51	3.47					
6	ETA	0.53	64.45	17.18	3.32	SPO	0.54	24.00	41.31	4.44					
7	SPO	0.95	24.00	118.80	5.01	SPO	0.96	24.00	39.60	3.48					
8	SPO	0.87	24.00	286.71	6.73	SPO	0.90	24.00	95.57	4.66					
9	SPO	0.62	24.00	125.62	4.85	SPO	0.67	24.00	41.87	3.36					
10	PER	0.45	57.03	20.40	3.19	PER	0.40	57.03	6.80	2.21					
11	PER	0.33	57.03	20.98	3.22	SDA	0.30	41.22	13.39	2.20					
12	CAP	0.40	24.06	96.59	4.45	CAP	0.38	24.06	32.20	3.08					
13	PER	0.44	57.03	206.63	6.90	PER	0.40	57.03	68.88	4.79					

Table 4 : Continued from previous page.

14	SPO	0.90	24.00	120.55	4.71	SPO	0.91	24.00	40.18	3.27
15	SPO	0.74	24.00	130.95	5.18	SPO	0.78	24.00	43.65	3.59
16	SPO	0.84	24.00	134.53	5.23	SPO	0.86	24.00	44.84	3.62
17	NIA	0.41	31.20	45.52	3.64	SPO	0.44	24.00	25.64	3.01
18	SPO	0.51	24.00	103.45	4.79	SPO	0.57	24.00	34.48	3.32
19	SPO	1.00	24.00	866.29	9.72	SPO	0.99	24.00	288.76	6.74
20	SPO	1.00	24.00	705.91	9.08	SPO	1.00	24.00	235.3	6.30
21	SPO	0.56	24.00	210.48	6.31	SPO	0.64	24.00	70.16	4.38
22	SPO	0.53	24.00	128.89	5.36	SPO	0.60	24.00	42.96	3.72
23	STA	0.51	28.55	51.32	3.94	STA	0.49	28.55	17.11	2.73
24	STA	0.46	27.83	138.03	5.48	STA	0.44	27.83	46.01	3.80
25	SPO	0.99	24.00	112.74	4.93	SPO	0.99	24.00	37.58	3.42
26	SPO	0.60	24.00	122.93	5.07	SPO	0.65	24.00	40.98	3.52
27	GEM	0.83	34.16	78.54	3.73	GEM	0.80	34.16	26.18	2.58
28	SPO	0.96	24.00	165.30	5.60	SPO	0.97	24.00	55.10	3.88
29	GEM	0.71	33.85	67.27	3.54	GEM	0.67	33.85	22.42	2.45
30	SPO	0.99	24.00	804.99	9.49	SPO	0.99	24.00	268.33	6.58

Table 4 : Continued from previous page.

31	SPO	0.99	24.00	133.85	5.22	SPO	1.00	24.00	44.62	3.62
32	SPO	1.00	24.00	210.41	6.07	SPO	1.00	24.00	70.14	4.21
33	SPO	0.72	24.00	366.63	7.30	SPO	0.76	24.00	122.21	5.06
34	SPO	0.91	24.00	196.24	5.93	SPO	0.92	24.00	65.41	4.11
35	SPO	0.83	24.00	177.94	5.74	SPO	0.86	24.00	59.31	3.98
36	SPO	0.63	24.00	183.31	5.79	SPO	0.68	24.00	61.10	4.02
37	SPO	0.98	24.00	691.57	9.02	SPO	0.99	24.00	230.52	6.25
38	SPO	0.96	24.00	85.08	4.49	SPO	0.97	24.00	28.36	3.11
39	SPO	0.52	24.00	202.90	5.45	SPO	0.57	24.00	67.63	3.78
40	SPO	0.95	24.00	576.97	7.94	SPO	0.96	24.00	192.32	5.51
41	SPO	0.97	24.00	102.15	4.77	SPO	0.97	24.00	34.05	3.31
42	PER	0.86	58.36	268.96	7.54	PER	0.81	58.36	89.65	5.23
43	SPO	0.93	24.00	116.01	4.97	SPO	0.94	24.00	38.67	3.45
44	SPO	0.90	24.00	184.83	5.28	SPO	0.92	24.00	61.61	3.66
45	SPO	0.95	24.00	76.67	4.05	SPO	0.95	24.00	25.56	2.81
46	PER	0.88	58.28	9.36	2.46	PER	0.84	58.28	3.12	1.71
47	PER	0.79	58.28	91.96	5.27	PER	0.72	58.28	30.65	3.65

Table 4 : Continued from previous page.

48	SPO	0.88	24.00	103.50	4.35	SPO	0.90	24.00	34.50	3.02	
49	SPO	0.72	24.00	71.53	4.23	SPO	0.76	24.00	23.84	2.94	
50	SPO	1.00	24.00	223.30	6.19	SPO	1.00	24.00	74.43	4.29	
51	SPO	1.00	24.00	2112.45	13.09	SPO	1.00	24.00	704.15	9.07	
52	SPO	1.00	24.00	209.76	6.06	SPO	1.00	24.00	69.92	4.20	
53	SPO	1.00	24.00	73.59	4.27	SPO	1.00	24.00	24.53	2.96	
54	SPO	1.00	24.00	65.62	4.11	SPO	1.00	24.00	21.87	2.85	
55	STA	0.54	30.02	153.37	5.68	STA	0.51	30.02	51.12	3.94	
56	SPO	1.00	24.00	141.53	5.32	SPO	1.00	24.00	47.18	3.69	
57	SPO	1.00	24.00	146.41	5.38	SPO	1.00	24.00	48.80	3.73	
58	SPO	0.87	24.00	391.96	7.46	SPO	0.89	24.00	130.65	5.18	
59	SPO	0.83	24.00	349.00	7.18	SPO	0.85	24.00	116.33	4.98	
60	SPO	0.86	24.00	306.39	6.88	SPO	0.87	24.00	102.13	4.77	
61	SPO	1.00	24.00	380.90	7.39	SPO	1.00	24.00	126.97	5.13	
62	SPO	0.94	24.00	283.37	6.70	SPO	0.95	24.00	94.46	4.65	
63	SPO	0.66	24.00	167.55	5.62	SPO	0.71	24.00	55.85	3.90	
64	SPO	0.77	24.00	170.14	5.65	SPO	0.81	24.00	56.71	3.92	

Table 4 : Continued from previous page.

65	SPO	0.78	24.00	3468.58	15.44	SPO	0.81	24.00	1156.19	10.7	
66	SPO	0.81	24.00	123.12	5.07	SPO	0.84	24.00	41.04	3.52	
67	SPO	0.90	24.00	241.83	6.35	SPO	0.92	24.00	80.61	4.41	
68	SPO	0.59	24.00	230.27	5.94	SPO	0.64	24.00	76.76	4.12	
69	SPO	0.92	24.00	1064.74	9.89	SPO	0.93	24.00	354.91	6.86	
70	CAP	0.42	22.70	237.62	6.00	CAP	0.39	22.7	79.21	4.16	
71	SPO	0.41	24.00	511.15	7.75	SPO	0.47	24.00	170.38	5.37	
72	SPO	0.48	24.00	199.86	5.66	SPO	0.54	24.00	66.62	3.93	
73	CAP	0.48	22.67	141.39	5.05	SPO	0.47	24.00	42.06	3.37	
74	CAP	0.42	22.67	285.40	6.38	SPO	0.43	24.00	84.85	4.26	
75	CAP	0.41	22.67	449.37	7.42	CAP	0.38	22.67	149.79	5.15	
76	SPO	0.36	24.00	141.93	5.05	SPO	0.41	24.00	47.31	3.50	
77	SPO	0.60	24.00	161.09	5.55	SPO	0.65	24.00	53.7	3.85	
78	CAP	0.42	22.62	115.55	4.72	CAP	0.40	22.62	38.52	3.27	
79	PER	0.34	56.98	16.91	3.00	PER	0.30	56.98	5.64	2.08	
80	PER	0.87	58.06	34.62	3.81	PER	0.82	58.06	11.54	2.64	
81	PER	0.90	58.06	83.49	5.10	PER	0.86	58.06	27.83	3.54	

Table 4 : Continued from previous page.

82	SPO	0.90	24.00	231.65	7.17	SPO	0.92	24.00	77.22	4.97
83	SPO	1.00	24.00	104.33	4.80	SPO	1.00	24.00	34.78	3.33
84	SPO	1.00	24.00	98.74	4.71	SPO	1.00	24.00	32.91	3.27
85	SPO	1.00	24.00	129.96	5.17	SPO	1.00	24.00	43.32	3.58
86	SPO	1.00	24.00	176.51	5.72	SPO	1.00	24.00	58.84	3.97
87	SPO	1.00	24.00	180.48	5.76	SPO	1.00	24.00	60.16	4.00
88	SPO	1.00	24.00	465.34	7.90	SPO	1.00	24.00	155.11	5.48
89	STA	0.37	27.22	108.21	5.05	STA	0.35	27.22	36.07	3.50
90	STA	0.44	26.87	168.73	5.86	STA	0.41	26.87	56.24	4.06
91	NTA	0.67	29.02	151.73	5.66	NTA	0.61	29.02	50.58	3.92
92	NTA	0.51	28.89	197.28	6.18	NTA	0.45	28.89	65.76	4.28
93	SPO	0.65	24.00	288.12	5.75	SPO	0.69	24.00	96.04	3.98
94	SPO	0.55	24.00	213663.59	60.98	SPO	0.59	24.00	71221.20	42.28
95	SPO	0.52	24.00	114.97	4.96	SPO	0.57	24.00	38.32	3.44
96	SPO	0.66	24.00	164.05	5.58	SPO	0.70	24.00	54.68	3.30
97	SPO	1.00	24.00	275.58	6.64	SPO	1.00	24.00	91.86	4.60
98	SPO	0.93	24.00	138.46	5.28	SPO	0.94	24.00	46.15	3.66

Table 4 : Continued from previous page.

99	SPO	0.96	24.00	115.94	4.97	SPO	0.97	24.00	38.65	3.45
100	SPO	0.99	24.00	623.57	8.71	SPO	0.99	24.00	207.86	6.04
101	SPO	1.00	24.00	189.94	5.86	SPO	1.00	24.00	63.31	4.07
102	SPO	1.00	24.00	139.18	5.29	SPO	1.00	24.00	46.39	3.66
103	SPO	1.00	24.00	94.03	4.64	SPO	1.00	24.00	31.34	3.22
104	SPO	1.00	24.00	144.02	5.35	SPO	1.00	24.00	48.01	3.71
105	HVI	0.61	18.65	500.83	8.10	HVI	0.55	18.65	166.94	5.62
106	SPO	0.93	24.00	798.44	9.46	SPO	0.94	24.00	266.15	6.56
107	SPO	0.94	24.00	174.23	5.70	SPO	0.95	24.00	58.08	3.95
108	SDA	0.68	42.16	32.90	2.97	SDA	0.63	42.16	10.97	2.06
109	SDA	0.67	42.16	77.35	3.95	SDA	0.62	42.16	25.78	2.74
110	SPO	0.95	24.00	154.33	5.47	SPO	0.96	24.00	51.44	3.79
111	SPO	0.54	24.00	247.32	6.40	SPO	0.59	24.00	82.44	4.44
112	SPO	0.72	24.00	135.93	4.90	SPO	0.74	24.00	45.31	3.40
113	SPO	0.74	24.00	19630.98	27.51	SPO	0.78	24.00	6543.66	19.08
114	SPO	0.74	24.00	123863.08	50.84	SPO	0.78	24.00	41287.69	35.25
115	SPO	0.74	24.00	123689.30	50.82	SPO	0.78	24.00	41229.77	35.24

Table 4 : Continued from previous page.

116	SPO	0.78	24.00	19630.98	27.51	SPO	0.81	24.00	6543.66	19.08	
117	SPO	0.84	24.00	12368.93	23.59	SPO	0.87	24.00	4122.98	16.35	
118	SPO	0.75	24.00	49241.60	37.38	SPO	0.79	24.00	16413.87	25.92	
119	SPO	0.63	24.00	3106.93	24.57	SPO	0.68	24.00	1035.64	17.04	
120	SPO	0.76	24.00	123689.30	50.82	SPO	0.79	24.00	41229.77	35.24	
121	SPO	0.73	24.00	7804.27	20.23	SPO	0.77	24.00	2601.42	14.03	
122	SPO	0.65	24.00	19603.43	27.50	SPO	0.70	24.00	6534.48	19.07	
123	SPO	0.55	24.00	7968.84	33.63	SPO	0.61	24.00	2656.28	23.32	
124	SPO	0.64	24.00	3172.45	14.99	SPO	0.69	24.00	1057.48	10.39	
125	SPO	0.72	24.00	3172.45	14.99	SPO	0.76	24.00	1057.48	10.39	
126	SPO	0.47	24.00	4942.91	28.68	SPO	0.53	24.00	1647.64	19.89	
127	SPO	0.52	24.00	3419.66	15.37	SPO	0.57	24.00	1139.89	10.65	
128	SPO	0.53	24.00	2594.08	14.01	SPO	0.58	24.00	864.69	9.72	
129	SPO	0.69	24.00	41113.32	35.20	SPO	0.74	24.00	13704.44	24.41	
130	SPO	0.68	24.00	5720.22	18.24	SPO	0.73	24.00	1906.74	12.65	
131	SPO	0.66	24.00	21275.62	28.26	SPO	0.71	24.00	7091.87	19.6	
132	SPO	1.00	24.00	4784.54	17.19	SPO	1.00	24.00	1594.85	11.92	

Table 4 : Continued from previous page.

133	SPO	0.92	24.00	2471.81	13.79	SPO	0.94	24.00	823.94	9.56
134	SPO	0.96	24.00	6587.62	19.12	SPO	0.96	24.00	2195.87	13.26
135	PER	0.77	58.82	59.20	4.55	PER	0.75	58.82	19.73	3.15
136	SPO	1.00	24.00	516.90	8.19	SPO	1.00	24.00	172.30	5.68
137	SPO	0.99	24.00	2596.77	14.02	SPO	0.99	24.00	865.59	9.72
138	SPO	0.95	24.00	471.42	7.94	SPO	0.96	24.00	157.14	5.50
139	SPO	0.95	24.00	6522.80	19.06	SPO	0.96	24.00	2174.27	13.21
140	SPO	0.72	24.00	3152.82	14.96	SPO	0.76	24.00	1050.94	10.37
141	SPO	0.53	24.00	1989.29	12.83	SPO	0.58	24.00	663.10	8.89
142	SPO	0.61	24.00	2489.15	13.82	SPO	0.66	24.00	829.72	9.58
143	SPO	0.91	24.00	2054.43	12.97	SPO	0.93	24.00	684.81	8.99
144	SPO	0.91	24.00	2054.43	12.97	SPO	0.93	24.00	684.81	8.99
145	SPO	1.00	24.00	1613.74	11.96	SPO	1.00	24.00	537.91	8.29
146	SPO	0.99	24.00	3080.33	14.84	SPO	0.99	24.00	1026.78	10.29
147	SPO	1.00	24.00	645.85	8.82	SPO	1.00	24.00	215.28	6.11
148	CAP	0.70	24.41	1439.74	10.94	CAP	0.66	24.41	479.91	7.59
149	NTA	0.45	31.87	1589.89	12.38	NTA	0.43	31.87	529.96	8.58

Table 4 : Continued from previous page.

150	STA	0.49	28.85	1116.71	11.01	STA	0.48	28.85	372.24	7.63	
151	SPO	0.48	24.00	2735.31	14.26	SPO	0.53	24.00	911.77	9.89	
152	SPO	0.98	24.00	569.44	8.45	SPO	0.99	24.00	189.81	5.86	
153	SPO	0.72	24.00	2986.11	14.69	SPO	0.77	24.00	995.37	10.18	
154	SPO	0.54	24.00	614.07	8.67	SPO	0.59	24.00	204.69	6.01	
155	AVB	0.51	20.03	2534.42	13.91	SPO	0.52	24.00	588.39	8.55	
156	AVB	0.59	20.02	2537.42	13.91	AVB	0.54	20.02	845.81	9.65	
157	AVB	0.57	19.97	882.34	9.78	AVB	0.52	19.97	294.11	6.78	
158	AVB	0.67	19.76	3719.26	15.80	AVB	0.63	19.76	1239.75	10.96	
159	PER	0.98	58.64	471.58	9.09	PER	0.97	58.64	157.19	6.30	
160	PER	0.92	58.64	93.86	5.31	PER	0.90	58.64	31.29	3.68	
161	PER	0.97	58.65	621.53	9.96	PER	0.96	58.65	207.18	6.91	
162	SPO	0.49	24.00	10978.34	22.67	SPO	0.54	24.00	3659.45	15.72	
163	SPO	0.44	24.00	4792.22	17.20	SPO	0.49	24.00	1597.41	11.92	
164	SPO	0.38	24.00	14472.27	24.86	SPO	0.43	24.00	4824.09	17.23	
165	SPO	0.56	24.00	489.88	8.04	SPO	0.61	24.00	163.29	5.57	
166	SPO	0.44	24.00	446.77	7.80	SPO	0.49	24.00	148.92	5.41	

Table 4 : Continued from previous page.

167	PER	0.60	59.05	7065.26	22.4	PER	0.54	59.05	2355.09	15.53					
168	SPO	0.48	24.00	933.44	9.97	SPO	0.53	24.00	311.15	6.91					
169	SPO	0.47	24.00	489.88	8.04	SPO	0.52	24.00	163.29	5.57					
170	PER	0.84	59.17	1115.00	12.11	PER	0.80	59.17	371.67	8.39					
171	GEM	0.53	36.97	1033.48	8.80	GEM	0.51	36.97	344.49	6.10					
172	SPO	0.65	24.00	1287.13	11.09	SPO	0.69	24.00	429.04	7.69					
173	SPO	0.44	24.00	4262.10	14.11	SPO	0.48	24.00	1420.7	9.78					
174	GEM	0.55	36.90	663.10	7.59	GEM	0.53	36.90	221.03	5.26					
175	GEM	0.69	36.92	2688.43	12.10	GEM	0.68	36.92	896.14	8.39					
176	SPO	0.93	24.00	2811.55	14.40	SPO	0.94	24.00	937.18	9.98					
177	SPO	0.89	24.00	5874.16	18.40	SPO	0.91	24.00	1958.05	12.76					
178	SPO	1.00	24.00	2430.56	13.71	SPO	1.00	24.00	810.19	9.51					
179	SPO	0.99	24.00	312.50	6.92	SPO	0.99	24.00	104.17	4.80					
180	SPO	1.00	24.00	5719.49	18.24	SPO	1.00	24.00	1906.5	12.65					
181	LEO	0.49	70.27	51.04	6.25	SPO	0.46	24.00	145.83	8.86					
182	SPO	1.00	24.00	148.61	5.40	SPO	1.00	24.00	14.86	2.51	SPO	1.00	24.00	57.56	3.94
183	SPO	1.00	24.00	218.06	6.14	SPO	1.00	24.00	21.81	2.85	SPO	1.00	24.00	84.46	4.48

Table 4 : Continued from previous page.

184	NTA	0.81	30.14	219.22	6.40	NTA	0.69	30.14	21.92	2.97	NTA	0.76	30.14	80.37	4.58
185	SPO	0.81	24.00	108.33	8.03	SPO	0.87	24.00	10.83	3.73	SPO	0.84	24.00	41.96	5.85
186	LEO	0.86	69.86	70.32	6.95	LEO	0.80	69.86	7.03	3.23	LEO	0.83	69.86	23.86	4.85
187	LEO	0.80	69.86	42.37	5.87	LEO	0.73	69.86	4.24	2.72	LEO	0.77	69.86	14.38	4.09
188	LEO	0.84	69.86	15.82	4.23	LEO	0.78	69.86	1.58	1.96	LEO	0.81	69.86	5.37	2.95
189	SPO	0.51	24.00	285.42	6.72	SPO	0.62	24.00	28.54	3.12	SPO	0.56	24.00	110.55	4.90
190	SPO	0.85	24.00	262.50	6.53	SPO	0.90	24.00	26.25	3.03	SPO	0.88	24.00	101.68	4.76
191	SPO	0.72	24.00	393.75	7.48	SPO	0.81	24.00	39.38	3.47	SPO	0.76	24.00	152.51	5.45
192	SPO	0.77	24.00	123.61	5.08	SPO	0.84	24.00	12.36	2.36	SPO	0.80	24.00	47.88	3.7
193	SPO	0.75	24.00	129.17	5.16	SPO	0.82	24.00	12.92	2.39	SPO	0.78	24.00	50.03	3.76
194	SPO	1.00	24.00	74.31	4.29	SPO	1.00	24.00	7.43	1.99	SPO	1.00	24.00	28.78	3.13
195	SPO	0.99	24.00	197.22	5.94	SPO	0.99	24.00	19.72	2.76	SPO	0.99	24.00	76.39	4.33
196	SPO	0.99	24.00	112.50	4.92	SPO	0.99	24.00	11.25	2.29	SPO	0.99	24.00	43.58	3.59
197	SPO	1.00	24.00	159.72	5.53	SPO	1.00	24.00	15.97	2.57	SPO	1.00	24.00	61.87	4.03
198	SPO	0.99	24.00	162.50	5.57	SPO	0.99	24.00	16.25	2.58	SPO	0.99	24.00	62.94	4.06
199	SPO	0.99	24.00	40.49	3.50	SPO	0.99	24.00	4.05	1.63	SPO	0.99	24.00	15.68	2.55
200	SPO	0.99	24.00	154.17	5.47	SPO	0.99	24.00	15.42	2.54	SPO	0.99	24.00	59.71	3.99

Table 4 : Continued from previous page.

201	SPO	1.00	24.00	420.14	7.64	SPO	1.00	24.00	42.01	3.55	SPO	1.00	24.00	162.74	5.57
202	SPO	1.00	24.00	250.69	6.43	SPO	1.00	24.00	25.07	2.99	SPO	1.00	24.00	97.10	4.69
203	SPO	1.00	24.00	91.67	4.60	SPO	1.00	24.00	9.17	2.13	SPO	1.00	24.00	35.51	3.35
204	SPO	0.80	24.00	69.10	4.19	SPO	0.86	24.00	6.91	1.94	SPO	0.82	24.00	26.76	3.05
205	SPO	0.45	24.00	70.83	4.22	SPO	0.65	24.00	7.08	1.96	SPO	0.55	24.00	27.44	3.08
206	LYR	0.52	47.16	88.85	4.55	SPO	0.58	24.00	34.31	3.31	SPO	0.48	24.00	132.88	5.20
207	LYR	0.46	47.25	198.9	5.95	SPO	0.62	24.00	77.08	4.34	SPO	0.51	24.00	298.57	6.82
208	LYR	0.50	47.25	36.91	3.40	SPO	0.58	24.00	14.31	2.48	SPO	0.47	24.00	55.41	3.89
209	SPO	0.58	24.00	204.86	6.01	SPO	0.75	24.00	20.49	2.79	SPO	0.66	24.00	79.35	4.38
210	LYR	0.88	47.21	47.37	3.69	LYR	0.77	47.21	4.74	1.71	LYR	0.84	47.21	16.42	2.59
211	LYR	0.79	47.20	28.91	3.13	LYR	0.64	47.20	2.89	1.45	LYR	0.73	47.20	10.02	2.20
212	SPO	0.82	24.00	136.81	5.26	SPO	0.87	24.00	13.68	2.44	SPO	0.84	24.00	52.99	3.83
213	LYR	0.72	47.22	59.56	3.98	LYR	0.54	47.22	5.96	1.85	LYR	0.64	47.22	20.64	2.80
214	LYR	0.69	47.22	36.96	3.40	LYR	0.51	47.22	3.70	1.58	LYR	0.62	47.22	12.81	2.39
215	LYR	0.79	47.22	18.30	2.69	LYR	0.64	47.22	1.83	1.25	LYR	0.73	47.22	6.34	1.89
216	LYR	0.69	47.22	151.24	5.43	LYR	0.51	47.22	15.12	2.52	LYR	0.61	47.22	52.41	3.82
217	LYR	0.60	47.22	83.07	4.45	SPO	0.52	24.00	32.15	3.24	LYR	0.51	47.22	28.78	3.13

Table 4 : Continued from previous page.

218	SPO	0.94	24.00	277.78	6.65	SPO	0.96	24.00	27.78	3.09	SPO	0.95	24.00	107.59	4.85
219	SPO	0.99	24.00	93.06	4.62	SPO	0.99	24.00	9.31	2.15	SPO	0.99	24.00	36.04	3.37
220	SPO	0.95	24.00	447.92	7.30	SPO	0.96	24.00	44.79	3.39	SPO	0.96	24.00	173.5	5.32
221	STA	0.65	30.80	85.15	4.67	SPO	0.50	24.00	14.03	2.56	STA	0.59	30.80	31.09	3.34
222	SPO	0.57	24.00	100.00	7.82	SPO	0.68	24.00	10.00	3.63	SPO	0.62	24.00	38.73	5.70
223	SPO	0.95	24.00	563.89	8.43	SPO	0.97	24.00	56.39	3.91	SPO	0.96	24.00	218.42	6.14
224	QUA	0.74	40.99	28.56	3.12	QUA	0.66	40.99	2.86	1.45	QUA	0.70	40.99	10.02	2.20
225	QUA	0.74	40.96	69.60	4.20	QUA	0.65	40.96	6.96	1.95	QUA	0.70	40.96	24.43	2.96
226	SPO	0.79	24.00	523.61	8.22	SPO	0.86	24.00	52.36	3.82	SPO	0.82	24.00	202.81	5.99
227	SPO	0.55	24.00	184.72	5.81	SPO	0.66	24.00	18.47	2.70	SPO	0.60	24.00	71.55	4.23
228	SPO	0.98	24.00	51.94	3.81	SPO	0.99	24.00	5.19	1.77	SPO	0.98	24.00	20.12	2.77
229	SPO	1.00	24.00	200.69	5.97	SPO	1.00	24.00	20.07	2.77	SPO	1.00	24.00	77.74	4.35
230	SPO	1.00	24.00	140.28	5.30	SPO	1.00	24.00	14.03	2.46	SPO	1.00	24.00	54.33	3.86
231	SPO	0.91	24.00	715.28	9.12	SPO	0.94	24.00	71.53	4.23	SPO	0.93	24.00	277.05	6.65
232	SPO	0.92	24.00	83.33	4.46	SPO	0.95	24.00	8.33	2.07	SPO	0.94	24.00	32.28	3.25
233	SPO	0.93	24.00	72.92	4.26	SPO	0.95	24.00	7.29	1.98	SPO	0.94	24.00	28.24	3.11
234	SPO	0.86	24.00	25.56	3.00	SPO	0.91	24.00	2.56	1.39	SPO	0.88	24.00	9.90	2.19

Table 4 : Continued from previous page.

235	SPO	0.91	24.00	318.75	6.97	SPO	0.94	24.00	31.88	3.23	SPO	0.92	24.00	123.46	5.08
236	SPO	0.73	24.00	1402.78	11.42	SPO	0.81	24.00	140.28	5.30	SPO	0.77	24.00	543.35	8.32
237	SPO	0.70	24.00	162.50	5.57	SPO	0.79	24.00	16.25	2.58	SPO	0.74	24.00	62.94	4.06
238	SPO	0.95	24.00	868.06	9.73	SPO	0.97	24.00	86.81	4.52	SPO	0.95	24.00	336.23	7.09
239	SPO	0.76	24.00	250.69	6.43	SPO	0.84	24.00	25.07	2.99	SPO	0.80	24.00	97.10	4.69
240	SPO	0.97	24.00	127.78	5.14	SPO	0.98	24.00	12.78	2.38	SPO	0.97	24.00	49.49	3.74
241	CAP	0.42	22.40	38.28	3.27	CAP	0.38	22.40	3.83	1.52	CAP	0.41	22.40	15.16	2.40
242	SPO	0.60	24.00	111.81	4.67	SPO	0.71	24.00	11.18	2.17	SPO	0.65	24.00	43.31	3.40
243	CAP	0.42	22.39	177.16	5.44	CAP	0.37	22.39	17.72	2.53	CAP	0.40	22.39	70.17	4.00
244	CAP	0.37	22.38	316.27	6.60	CAP	0.34	22.38	31.63	3.06	CAP	0.36	22.38	125.29	4.85
245	SPO	1.00	24.00	101.39	4.76	SPO	1.00	24.00	10.14	2.21	SPO	1.00	24.00	39.27	3.47
246	SPO	1.00	24.00	1097.22	10.52	SPO	1.00	24.00	109.72	4.88	SPO	1.00	24.00	425.00	7.67
247	ORI	0.30	65.98	31.70	4.07	SPO	0.39	24.00	23.96	3.70	SPO	0.33	24.00	92.80	5.82
248	STA	0.33	27.05	123.54	5.28	SPO	0.33	24.00	15.69	2.66	STA	0.31	27.05	46.35	3.81
249	SPO	0.32	24.00	97.22	5.91	SPO	0.43	24.00	9.72	2.74	SPO	0.37	24.00	37.66	4.31
250	STA	0.27	27.13	78.24	4.54	SPO	0.37	24.00	10.00	2.29	SPO	0.31	24.00	38.73	3.59
251	NTA	0.74	28.66	76.96	4.51	NTA	0.67	28.66	7.70	2.09	NTA	0.71	28.66	28.50	3.24

Table 4 : Continued from previous page.

252	SPO	0.57	24.00	304.17	6.86	SPO	0.67	24.00	30.42	3.18	SPO	0.61	24.00	117.82	5.00
253	SPO	0.51	24.00	100.69	4.75	SPO	0.62	24.00	10.07	2.20	SPO	0.55	24.00	39.00	3.46
254	AND	0.48	19.20	238.73	6.33	SPO	0.55	24.00	15.28	2.53	SPO	0.48	24.00	59.18	3.97
255	SPO	0.42	24.00	150.00	5.42	SPO	0.54	24.00	15.00	2.52	SPO	0.46	24.00	58.10	3.95
256	SPO	0.50	24.00	390.28	7.45	SPO	0.61	24.00	39.03	3.46	SPO	0.54	24.00	151.17	5.43
257	AND	0.66	19.01	588.86	8.55	AND	0.58	19.01	58.89	3.97	AND	0.63	19.01	249.36	6.42
258	AND	0.55	19.00	151.79	5.44	AND	0.46	19.00	15.18	2.53	AND	0.52	19.00	64.29	4.09
259	AND	0.65	18.96	832.64	9.60	AND	0.54	18.96	83.26	4.45	AND	0.61	18.96	353.08	7.21
260	AND	0.46	18.95	104.77	4.81	SPO	0.47	24.00	6.53	1.91	AND	0.43	18.95	44.43	3.61
261	AND	0.67	19.00	396.78	7.49	AND	0.58	19.00	39.68	3.48	AND	0.64	19.00	168.08	5.63
262	SPO	0.96	24.00	124.31	5.09	SPO	0.98	24.00	12.43	2.36	SPO	0.97	24.00	48.15	3.71
263	SPO	0.67	24.00	285.42	6.72	SPO	0.76	24.00	28.54	3.12	SPO	0.71	24.00	110.55	4.90
264	SPO	0.54	24.00	120.83	5.04	SPO	0.65	24.00	12.08	2.34	SPO	0.59	24.00	46.80	3.68
265	SPO	0.72	24.00	86.81	4.52	SPO	0.80	24.00	8.68	2.10	SPO	0.75	24.00	33.62	3.29
266	SPO	0.49	24.00	35.28	3.35	SPO	0.61	24.00	3.53	1.55	SPO	0.53	24.00	13.66	2.44
267	DPC	0.46	17.32	490.83	8.05	SPO	0.53	24.00	25.56	3.00	SPO	0.45	24.00	98.99	4.72
268	SPO	0.91	24.00	67.15	4.15	SPO	0.94	24.00	6.72	1.92	SPO	0.92	24.00	26.01	3.02

Table 4 : Continued from previous page.

269	SPO	0.90	24.00	103.47	4.79	SPO	0.93	24.00	10.35	2.22	SPO	0.91	24.00	40.08	3.49
270	SPO	0.91	24.00	112.5	4.92	SPO	0.94	24.00	11.25	2.29	SPO	0.92	24.00	43.58	3.59
271	SPO	1.00	24.00	75.69	4.31	SPO	1.00	24.00	7.57	2.00	SPO	1.00	24.00	29.32	3.15
272	SPO	1.00	24.00	124.31	5.09	SPO	1.00	24.00	12.43	2.36	SPO	1.00	24.00	48.15	3.71
273	SPO	1.00	24.00	241.67	6.35	SPO	1.00	24.00	24.17	2.95	SPO	1.00	24.00	93.61	4.63
274	SPO	1.00	24.00	173.61	5.69	SPO	1.00	24.00	17.36	2.64	SPO	1.00	24.00	67.25	4.15
275	SPO	1.00	24.00	736.11	9.21	SPO	1.00	24.00	73.61	4.27	SPO	0.99	24.00	285.12	6.71
276	SPO	1.00	24.00	393.75	7.48	SPO	1.00	24.00	39.38	3.47	SPO	1.00	24.00	152.51	5.45
277	SPO	0.93	24.00	339.58	7.12	SPO	0.96	24.00	33.96	3.30	SPO	0.94	24.00	131.53	5.19
278	STA	0.37	28.24	89.81	4.75	SPO	0.34	24.00	12.43	2.46	STA	0.35	28.24	33.37	3.42
279	STA	0.40	28.23	19.52	2.86	STA	0.35	28.23	1.95	1.33	STA	0.38	28.23	7.25	2.05
280	STA	0.40	28.27	79.59	4.56	STA	0.35	28.27	7.96	2.12	STA	0.38	28.27	29.56	3.28
281	STA	0.37	28.26	44.58	3.76	STA	0.33	28.26	4.46	1.75	STA	0.36	28.26	16.56	2.70
282	STA	0.43	28.26	96.68	4.87	STA	0.38	28.26	9.67	2.26	STA	0.41	28.26	35.91	3.50
283	STA	0.39	28.26	167.82	5.85	STA	0.35	28.26	16.78	2.72	STA	0.37	28.26	62.34	4.21
284	STA	0.43	28.25	89.24	4.74	STA	0.38	28.25	8.92	2.20	STA	0.41	28.25	33.15	3.41
285	STA	0.41	28.25	108.29	5.06	STA	0.37	28.25	10.83	2.35	STA	0.39	28.25	40.23	3.63

Table 4 : Continued from previous page.

286	STA	0.37	28.24	174.53	5.93	SPO	0.33	24.00	24.17	3.07	STA	0.35	28.24	64.84	4.26
287	SPO	0.87	24.00	162.50	9.19	SPO	0.91	24.00	16.25	4.27	SPO	0.89	24.00	62.94	6.70
288	SPO	0.86	24.00	262.50	10.78	SPO	0.91	24.00	26.25	5.00	SPO	0.89	24.00	101.68	7.86
289	GEM	0.86	34.55	75.07	3.67	GEM	0.81	34.55	7.51	1.70	GEM	0.84	34.55	26.90	2.61
290	SPO	0.99	24.00	330.56	7.05	SPO	0.99	24.00	33.06	3.27	SPO	0.99	24.00	128.04	5.14
291	SPO	0.98	24.00	144.44	5.35	SPO	0.99	24.00	14.44	2.48	SPO	0.99	24.00	55.95	3.90
292	SPO	1.00	24.00	108.33	4.86	SPO	1.00	24.00	10.83	2.26	SPO	1.00	24.00	41.96	3.54
293	SPO	1.00	24.00	167.36	5.62	SPO	1.00	24.00	16.74	2.61	SPO	1.00	24.00	64.83	4.10
294	SPO	0.69	24.00	103.47	4.79	SPO	0.81	24.00	10.35	2.22	SPO	0.75	24.00	40.08	3.49
295	SPO	0.99	24.00	97.22	4.69	SPO	0.99	24.00	9.72	2.18	SPO	0.99	24.00	37.66	3.42
296	SPO	0.99	24.00	49.10	3.73	SPO	1.00	24.00	4.91	1.73	SPO	1.00	24.00	19.02	2.72
297	SPO	0.99	24.00	362.5	7.27	SPO	0.99	24.00	36.25	3.38	SPO	0.99	24.00	140.41	5.30
298	SPO	0.91	24.00	3527.78	15.53	SPO	0.94	24.00	352.78	7.21	SPO	0.93	24.00	1366.44	11.32
299	SPO	1.00	24.00	173.61	5.69	SPO	1.00	24.00	17.36	2.47	SPO	1.00	24.00	67.25	3.88
300	SPO	1.00	24.00	202.78	5.99	SPO	1.00	24.00	20.28	2.78	SPO	1.00	24.00	78.54	4.37
301	SPO	0.98	24.00	165.97	5.61	SPO	0.99	24.00	16.6	2.6	SPO	0.99	24.00	64.29	4.09
302	SPO	1.00	24.00	102.78	4.78	SPO	1.00	24.00	10.28	2.22	SPO	1.00	24.00	39.81	3.48

Table 4 : Continued from previous page.

303	SPO	1.00	24.00	105.56	4.82	SPO	1.00	24.00	10.56	2.24	SPO	1.00	24.00	40.89	3.51
304	SPO	0.87	24.00	427.78	7.69	SPO	0.92	24.00	42.78	3.57	SPO	0.90	24.00	165.69	5.60
305	SPO	1.00	24.00	1083.33	10.48	SPO	1.00	24.00	108.33	4.86	SPO	1.00	24.00	419.62	7.64
306	SPO	0.99	24.00	107.64	4.85	SPO	1.00	24.00	10.76	2.25	SPO	0.99	24.00	41.69	3.54
307	SPO	1.00	24.00	86.81	4.52	SPO	1.00	24.00	8.68	2.10	SPO	1.00	24.00	33.62	3.29

Appendix A. Additional data tables

Table A.5: NC are the nominal NELIOTA coordinates as described in §2 and UC the updated ones as derived in this work.

ID	Long.NC	Lat.NC	Long.UC	Lat.UC	ID	Long.NC	Lat.NC	Long.UC	Lat.UC
1	-1.5	-29.2	-1.01	-29.09	29	13.0	50.0	10.49	52.28
2	-10.3	-9.7	-8.93	-9.70	30	-36.9	73.4	-42.58	73.28
3	4.5	-29.9	-12.79	-29.62	31	-40.7	79.2	-44.93	78.88
4	-12.7	-58.9	-10.58	-59.611	32	-1.4	-52.0	0.99	-49.80
5	11.6	-58.8	13.92	-58.26	33	21.7	74.5	22.81	74.775
6	4.7	-43.2	5.978	-44.89	34	4.3	24.6	6.92	25.47
7	26.8	-22.5	26.99	-22.96	35	3.6	-59.0	2.18	-59.60
8	5.6	0.0	11.09	-1.25	36	17.4	-58.2	18.96	-56.42
9	7.8	35.0	10.55	35.95	37	2.5	-20.0	2.21	-15.36
10	-3.2	-40.0	-5.18	-38.96	38	24.9	46.0	27.71	46.69
11	28.5	-30.6	29.02	-30.76	39	-22.1	10.6	-18.93	11.26
12	20.6	-50.7	19.42	-52.80	40	28.8	67.2	32.76	69.50
13	18.1	-18.7	22.05	-20.87	41	1.8	52.1	4.461	53.39
14	32.0	47.5	35.09	48.07	42	3.1	70.0	6.21	71.25
15	6.7	68.1	10.45	70.93	43	26.7	60.2	29.60	61.38
16	-15.6	34.6	-12.10	36.53	44	10.3	30.6	12.24	31.33
17	-25.9	57.8	18.44	77.82	45	21.9	34.9	23.30	35.93
18	13.5	76.8	-23.42	59.14	46	28.0	76.4	28.64	80.49
19	-1.1	70.0	0.65	69.45	47	26.6	60.2	28.46	62.62
20	24.7	52.5	26.86	52.13	48	13.2	10.3	13.81	11.149
21	-17.3	65.2	-18.18	65.63	49	11.7	-62.4	10.00	-62.03
22	-12.5	66.5	-11.68	66.22	50	-24.7	29.2	-22.77	31.10
23	-25.4	72.5	-27.05	74.11	51	9.5	52.1	11.03	55.44
24	-27.9	-33.8	-19.99	-30.72	52	-15.5	15.2	-14.40	17.35
25	-29.5	64.4	-31.11	61.27	53	-18.6	72.5	-18.28	76.22

Table A.5 : Continued from previous page.

26	-35.0	-30.5	-34.92	-29.39	54	0.0	60.8	0.79	62.66
27	9.0	74.0	5.34	74.08	55	5.5	-53.3	4.72	-53.62
28	5.4	51.2	3.46	51.88	56	-36.0	-43.1	-32.60	-44.57
57	-21.6	-93.3	-15.85	-85.71	83	9.1	42.7	9.53	43.19
58	25.9	-33.3	27.29	-31.49	84	-17.2	33.9	-17.82	33.60
59	28.7	-57.4	26.95	-59.79	85	-22.5	-65.9	-23.92	-66.95
60	-7.6	-83.3	-9.59	-81.24	86	-4.8	-53.0	-6.13	-51.86
61	4.3	15.5	5.93	16.82	87	-31.8	25.6	-31.45	34.11
62	33.2	21.2	35.00	20.51	88	12.5	17.8	12.619	20.31
63	25.7	-6.8	24.99	-7.62	89	-1.6	65.3	-3.49	68.63
64	35.7	-77.5	38.31	-77.70	90	-5.7	55.0	-8.86	55.91
65	34.4	-57.5	35.74	-58.04	91	-33.9	-48.3	-35.47	-54.98
66	33.7	-70.9	29.58	-70.13	92	12.1	-25.3	9.40	-26.46
67	8.6	-83.0	5.66	-81.18	93	-16.7	3.3	-17.30	3.11
68	-11.0	53.3	-6.67	54.74	94	-13.1	-23.1	-11.42	-22.11
69	-9.3	40.8	-5.83	41.99	95	16.5	-40.7	17.96	-38.89
70	18.5	60.5	20.50	62.58	96	-28.6	-32.4	-28.08	-32.31
71	42.3	50.4	44.31	51.17	97	-39.8	48.7	-41.11	57.45
72	26.0	35.7	27.67	36.38	98	21.9	-46.5	21.04	-46.25
73	0.5	49.4	3.14	51.28	99	-39.1	-40.4	-36.71	-41.35
74	19.9	49.8	22.39	51.47	100	-7.8	-45.1	-3.95	-44.183
75	17.4	60.8	19.63	63.34	101	-30.6	-31.3	-27.47	-31.22
76	31.7	24.2	32.71	25.39	102	-1.9	-32.1	-0.683	-32.25
77	21.2	4.2	22.20	5.22	103	15.1	-91.3	14.30	-89.73
78	11.2	60.5	13.52	61.60	104	-22.7	-42.8	-21.48	-43.26
79	2.9	74.2	5.46	74.15	105	-26.6	-47.7	-27.49	-46.31
80	18.7	-26.3	31.26	-29.10	106	10.8	-46.5	8.79	-47.146
81	23.0	-7.3	31.62	-9.17	107	12.7	-24.9	12.02	-24.99

Table A.5 : Continued from previous page.

82	41.0	-56.0	39.63	-57.95			
----	------	-------	-------	--------	--	--	--

Table A.6: Origin for NELIOTA impactors are estimated by using the nominal NELIOTA coordinates (NC) as described in §2 and the updated ones as derived in this work (UC), for $\eta_1 = 5 \times 10^{-4}$ and $\eta_2 = 1.5 \times 10^{-3}$.

ID	NC	NC	UC	UC	ID	NC	NC	UC	UC
	η_1	η_2	η_1	η_2		η_1	η_2	η_1	η_2
1	SPO	SPO	SPO	SPO	29	GEM	GEM	GEM	GEM
2	SPO	SPO	SPO	SPO	30	SPO	SPO	SPO	SPO
3	SPO	SPO	SPO	SPO	31	SPO	SPO	SPO	SPO
4	SPO	SPO	SPO	SPO	32	SPO	SPO	SPO	SPO
5	SPO	SPO	SPO	SPO	33	SPO	SPO	SPO	SPO
6	ETA	SPO	ETA	SPO	34	SPO	SPO	SPO	SPO
7	SPO	SPO	SPO	SPO	35	SPO	SPO	SPO	SPO
8	SPO	SPO	SPO	SPO	36	SPO	SPO	SPO	SPO
9	SPO	SPO	SPO	SPO	37	SPO	SPO	SPO	SPO
10	PER	PER	PER	PER	38	SPO	SPO	SPO	SPO
11	PER	SDA	PER	SDA	39	SPO	SPO	SPO	SPO
12	CAP	CAP	CAP	CAP	40	SPO	SPO	SPO	SPO
13	PER	PER	PER	PER	41	SPO	SPO	SPO	SPO
14	SPO	SPO	SPO	SPO	42	PER	PER	PER	PER
15	SPO	SPO	SPO	SPO	43	SPO	SPO	SPO	SPO
16	SPO	SPO	SPO	SPO	44	SPO	SPO	SPO	SPO
17	SPO	SPO	NIA	SPO	45	SPO	SPO	SPO	SPO
18	NIA	SPO	SPO	SPO	46	PER	PER	PER	PER
19	SPO	SPO	SPO	SPO	47	PER	PER	PER	PER
20	SPO	SPO	SPO	SPO	48	SPO	SPO	SPO	SPO
21	SPO	SPO	SPO	SPO	49	SPO	SPO	SPO	SPO
22	SPO	SPO	SPO	SPO	50	SPO	SPO	SPO	SPO
23	STA	STA	STA	STA	51	SPO	SPO	SPO	SPO
24	STA	STA	STA	STA	52	SPO	SPO	SPO	SPO
25	SPO	SPO	SPO	SPO	53	SPO	SPO	SPO	SPO

Table A.6 : Continued from previous page.

26	SPO	SPO	SPO	SPO	54	SPO	SPO	SPO	SPO
27	GEM	GEM	GEM	GEM	55	STA	STA	STA	STA
28	SPO	SPO	SPO	SPO	56	SPO	SPO	SPO	SPO
57	SPO	SPO	SPO	SPO	85	SPO	SPO	SPO	SPO
58	SPO	SPO	SPO	SPO	86	SPO	SPO	SPO	SPO
59	SPO	SPO	SPO	SPO	87	SPO	SPO	SPO	SPO
60	SPO	SPO	SPO	SPO	88	SPO	SPO	SPO	SPO
61	SPO	SPO	SPO	SPO	89	STA	STA	STA	STA
62	SPO	SPO	SPO	SPO	90	STA	STA	STA	STA
63	SPO	SPO	SPO	SPO	91	NTA	NTA	NTA	NTA
64	SPO	SPO	SPO	SPO	92	NTA	NTA	NTA	NTA
65	SPO	SPO	SPO	SPO	93	SPO	SPO	SPO	SPO
66	SPO	SPO	SPO	SPO	94	SPO	SPO	SPO	SPO
67	SPO	SPO	SPO	SPO	95	SPO	SPO	SPO	SPO
68	SPO	SPO	SPO	SPO	96	SPO	SPO	SPO	SPO
69	SPO	SPO	SPO	SPO	97	SPO	SPO	SPO	SPO
70	CAP	CAP	CAP	CAP	98	SPO	SPO	SPO	SPO
71	SPO	SPO	SPO	SPO	99	SPO	SPO	SPO	SPO
72	SPO	SPO	SPO	SPO	100	SPO	SPO	SPO	SPO
73	CAP	SPO	CAP	SPO	101	SPO	SPO	SPO	SPO
74	CAP	SPO	CAP	SPO	102	SPO	SPO	SPO	SPO
75	CAP	CAP	CAP	CAP	103	SPO	SPO	SPO	SPO
76	SPO	SPO	SPO	SPO	104	SPO	SPO	SPO	SPO
77	SPO	SPO	SPO	SPO	105	HVI	HVI	HVI	HVI
78	CAP	CAP	CAP	CAP	106	SPO	SPO	SPO	SPO
79	PER	PER	PER	PER	107	SPO	SPO	SPO	SPO
80	PER	PER	PER	PER	108	SDA	SDA	SDA	SDA
81	PER	PER	PER	PER	109	SDA	SDA	SDA	SDA
82	SPO	SPO	SPO	SPO	110	SPO	SPO	SPO	SPO

Table A.6 : Continued from previous page.

83	SPO	SPO	SPO	SPO	111	SPO	SPO	SPO	SPO
84	SPO	SPO	SPO	SPO	112	SPO	SPO	SPO	SPO

References

- Ait Moulay Larbi, M., Daassou, A., Baratoux, D., Bouley, S., Benkhaldoun, Z., Lazrek, M., Garcia, R., & Colas, F. (2015). First Lunar Flashes Observed from Morocco (ILIAD Network): Implications for Lunar Seismology. *Earth Moon and Planets*, 115, 1–21. doi:10.1007/s11038-015-9462-1.
- Arakawa, M., Saiki, T., Wada, K., Ogawa, K., Kadono, T., Shirai, K., Sawada, H., Ishibashi, K., Honda, R., Sakatani, N., Iijima, Y., Okamoto, C., Yano, H., Takagi, Y., Hayakawa, M., Michel, P., Jutzi, M., Shimaki, Y., Kimura, S., Mimasu, Y., Toda, T., Imamura, H., Nakazawa, S., Hayakawa, H., Sugita, S., Morota, T., Kameda, S., Tatsumi, E., Cho, Y., Yoshioka, K., Yokota, Y., Matsuoka, M., Yamada, M., Kouyama, T., Honda, C., Tsuda, Y., Watanabe, S., Yoshikawa, M., Tanaka, S., Terui, F., Kikuchi, S., Yamaguchi, T., Ogawa, N., Ono, G., Yoshikawa, K., Takahashi, T., Takei, Y., Fujii, A., Takeuchi, H., Yamamoto, Y., Okada, T., Hirose, C., Hosoda, S., Mori, O., Shimada, T., Soldini, S., Tsukizaki, R., Iwata, T., Ozaki, M., Abe, M., Namiki, N., Kitazato, K., Tachibana, S., Ikeda, H., Hirata, N., Hirata, N., Noguchi, R., & Miura, A. (2020). An artificial impact on the asteroid (162173) Ryugu formed a crater in the gravity-dominated regime. *Science*, 368, 67–71. doi:10.1126/science.aaz1701.
- Avdellidou, C., Di Donna, A., Schultz, C., Harthong, B., Price, M. C., Peyroux, R., Britt, D., Cole, M., & Delbo', M. (2020). Very weak carbonaceous asteroid simulants I: Mechanical properties and response to hypervelocity impacts. *Icarus*, 341, 113648. doi:10.1016/j.icarus.2020.113648.

- Avdellidou, C., Price, M. C., Delbo, M., & Cole, M. J. (2017). Survival of the impactor during hypervelocity collisions - II. An analogue for high-porosity targets. *MNRAS*, *464*, 734–738. doi:10.1093/mnras/stw2381. arXiv:1612.05060.
- Avdellidou, C., Price, M. C., Delbo, M., Ioannidis, P., & Cole, M. J. (2016). Survival of the impactor during hypervelocity collisions - I. An analogue for low porosity targets. *MNRAS*, *456*, 2957. doi:10.1093/mnras/stv2844. arXiv:1512.03262.
- Avdellidou, C., & Vaubaillon, J. (2019). Temperatures of lunar impact flashes: mass and size distribution of small impactors hitting the Moon. *Monthly Notices of the Royal Astronomical Society*, *484*, 5212–5222. doi:10.1093/mnras/stz355. arXiv:1902.00987.
- Babadzhanov, P. B., & Kokhirova, G. I. (2009). Densities and porosities of meteoroids. *Astronomy & Astrophysics*, *495*, 353–358. doi:10.1051/0004-6361:200810460.
- Baldwin, R. B. (1971). On the History of Lunar Impact Cratering: The Absolute Time Scale and the Origin of Planetesimals. *Icarus*, *14*, 36–52. doi:10.1016/0019-1035(71)90100-X.
- Ballouz, R. L., Walsh, K. J., Barnouin, O. S., DellaGiustina, D. N., Al Asad, M., Jawin, E. R., Daly, M. G., Bottke, B. F., Michel, P., Avdellidou, C., Delbo, M., Daly, R. T., Asphaug, E., Bennett, C. A., Bierhaus, E. B., Connolly Jr, H. C., Golish, D. R., Molaro, J. L., Nolan, M. C., Pajola, M., Rizk, B., Schwartz, S. R., Trang, D., & Wolner, D. S., C. W. V. & Lauretta (2020). Bennu's near-Earth lifetime of 1.75 million years inferred from craters on its boulders. *Science*, *587*, 205–209. doi:<https://doi.org/10.1126/science.abb3033>.
- Bellot Rubio, L. R., Ortiz, J. L., & Sada, P. V. (2000). Observation and Interpretation of Meteoroid Impact Flashes on the Moon. *Earth Moon and Planets*, *82*, 575–598.
- Bertin, E., & Arnouts, S. (1996). SExtractor: Software for source extraction. *Astronomy & Astrophysics*, *117*, 393. doi:10.1051/aas:1996164.

- Bessell, M. S., Castelli, F., & Plez, B. (1998). Model atmospheres broad-band colors, bolometric corrections and temperature calibrations for O - M stars. *Astronomy & Astrophysics*, 333, 231–250.
- Bonanos, A. Z., Avdellidou, C., Liakos, A., Xilouris, E. M., Dapergolas, A., Koschny, D., Bellas- Velidis, I., Boumis, P., Charmandaris, V., Fytsilis, A., & Maroussis, A. (2018). NELIOTA: First temperature measurement of lunar impact flashes. *Astronomy & Astrophysics*, 612. doi:10.1051/0004-6361/201732109.
- Bottke, W. F., Morbidelli, A., Jedicke, R., Petit, J.-M., Levison, H. F., Michel, P., & Metcalfe, T. S. (2002). Debiased Orbital and Absolute Magnitude Distribution of the Near-Earth Objects. *Icarus*, 156, 399–433. doi:10.1006/icar.2001.6788.
- Bouley, S., Baratoux, D., Vaubaillon, J., Mocquet, A., Le Feuvre, M., Colas, F., Benkhaldoun, Z., Daassou, A., Sabil, M., & Lognonné, P. (2012). Power and duration of impact flashes on the Moon: Implication for the cause of radiation. *Icarus*, 218, 115–124. doi:10.1016/j.icarus.2011.11.028.
- Burchell, M. J., Cole, M. J., Ramkissoon, N. K., Wozniakiewicz, P. J., Price, M. C., & Foing, B. (2015). SMART-1 end of life shallow regolith impact simulations. *Meteoritics and Planetary Science*, 50, 1436–1448. doi:10.1111/maps.12479.
- Cheng, A. F., Michel, P., Jutzi, M., Rivkin, A. S., Stickle, A., Barnouin, O., Ernst, C., Atchison, J., Pravec, P., Richardson, D. C., & AIDA Team (2016). Asteroid Impact & Deflection Assessment mission: Kinetic impactor. *Planetary & Space Science*, 121, 27–35. doi:10.1016/j.pss.2015.12.004.
- Cintala, M. J. (1992). Impact-induced thermal effects in the lunar and Mercurian regoliths. *Journal of Geophysical Research*, 97, 947–973. doi:10.1029/91JE02207.
- Colaprete, A., Schultz, P., Heldmann, J., Wooden, D., Shirley, M., Ennico, K., Hermalyn, B., Marshall, W., Ricco, A., Elphic, R. C., Goldstein, D., Summy, D., Bart, G. D., Asphaug, E., Korycansky, D., Landis, D., & Sollitt, L. (2010). Detection of Water in the LCROSS Ejecta Plume. *Science*, 330, 463. doi:10.1126/science.1186986.

Cudnik, B. (2009). *Lunar Meteoroid Impacts and How to Observe Them*. doi:10.1007/978-1-4419-0324-2.

Cudnik, B. M., Dunham, D. W., Palmer, D. M., Cook, A., Venable, R., & Gural, P. S. (2003). Ground-Based Observations Of Lunar Meteoritic Phenomena. *Earth Moon and Planets*, 93, 145–161. doi:10.1023/B:MOON.0000047475.61749.c1.

Daly, R. T., & Schultz, P. H. (2015). New Constraints on the Delivery of Impactors to Icy Bodies: Implications for Ceres. In *Lunar and Planetary Science Conference* (p. 1972). volume 46.

Daly, R. T., & Schultz, P. H. (2016). Delivering a projectile component to the vestan regolith. *Icarus*, 264, 9. doi:10.1016/j.icarus.2015.08.034.

Dunham, D. W., Sterner, I., Ray, Gotwols, B., Cudnik, B. M., Palmer, D. M., Sada, P. V., & Frankenberger, R. (2000). Confirmed lunar meteor impacts from the November 1999 Leonids. *Occultation Newsletter, International Occultation Timing Association (IOTA)*, 8, 9–11.

Eichhorn, G. (1975). Measurements of the light flash produced by high velocity particle impact. *Planetary & Space Science*, 23, 1519–1525. doi:10.1016/0032-0633(75)90005-7.

Eichhorn, G. (1976). Analysis of the hypervelocity impact process from impact flash measurements. *Planetary & Space Science*, 24, 771–781. doi:10.1016/0032-0633(76)90114-8.

Flynn, G. J., Durda, D. D., Molesky, M. J., May, B. A., Congram, S. N., Loftus, C. L., Reagan, J. R., Strait, M. M., & Macke, R. J. (2020). Hypervelocity cratering and disruption of the Northwest Africa 4502 carbonaceous chondrite meteorite: Implications for crater production, catastrophic disruption, momentum transfer and dust production on asteroids. *Planetary & Space Science*, 187, 104916. doi:10.1016/j.pss.2020.104916.

- Flynn, G. J., Durda, D. D., Patmore, E. B., Jack, S. J., Molesky, M. J., May, B. A., Congram, S. N., Strait, M. M., & Macke, R. J. (2018). Hypervelocity cratering and disruption of the Northwest Africa 869 ordinary chondrite meteorite: Implications for crater production, catastrophic disruption, momentum transfer and dust production on asteroids. *Planetary & Space Science*, *164*, 91–105. doi:10.1016/j.pss.2018.06.019.
- Foing, B. H., Racca, G., Marini, A., Koschny, D., Frew, D., Grieger, B., Camino-Ramos, O., Josset, J. L., Grande, M., Smart-1 Science, & Technology Working Team (2018). SMART-1 technology, scientific results and heritage for future space missions. *Planetary & Space Science*, *151*, 141–148. doi:10.1016/j.pss.2017.09.002.
- Halliday, I., Griffin, A. A., & Blackwell, A. T. (1996). Detailed data for 259 fireballs from the Canadian camera network and inferences concerning the influx of large meteoroids. *Meteoritics and Planetary Science*, *31*, 185–217. doi:10.1111/j.1945-5100.1996.tb02014.x.
- Hartmann, W. K., & Neukum, G. (2001). Cratering Chronology and the Evolution of Mars. *Space Science Reviews*, *96*, 165–194. doi:10.1023/A:1011945222010.
- Hayne, P. O., Greenhagen, B. T., Foote, M. C., Siegler, M. A., Vasavada, A. R., & Paige, D. A. (2010). Diviner Lunar Radiometer Observations of the LCROSS Impact. *Science*, *330*, 477. doi:10.1126/science.1197135.
- Holsapple, K. A. (1994). Catastrophic disruptions and cratering of solar system bodies: a review and new results. *Planetary & Space Science*, *42*, 1067–1078. doi:10.1016/0032-0633(94)90007-8.
- Hughes, D. W. (1987). P/Halley dust characteristics - A comparison between Oriroid and Eta Aquarid meteor observations and those from the flyby spacecraft. *Astronomy & Astrophysics*, *187*, 879–888.
- Ivanov, B. A. (2001). Mars/Moon Cratering Rate Ratio Estimates. *Space Science Reviews*, *96*, 87–104.

- Jenniskens, P. (1994). Meteor stream activity I. The annual streams. *Astronomy & Astrophysics*, 287, 990–1013.
- Jenniskens, P. (2006). *Meteor Showers and their Parent Comets*.
- Kopal, Z. (1965). Topography of the Moon. *Space Science Reviews*, 4, 737–855. doi:10.1007/BF00216275.
- Korycansky, D. G., & Zahnle, K. J. (2005). Modeling crater populations on Venus and Titan. *Planetary & Space Science*, 53, 695–710. doi:10.1016/j.pss.2005.03.002.
- Larson, R., Hayne, P., & Avdellidou, C. (2019). Automating the detection and coordinate identification of impact flashes on the Lunar surface. In *EPSC-DPS Joint Meeting 2019* (pp. EPSC–DPS2019–1193). volume 2019.
- Le Feuvre, M., & Wieczorek, M. A. (2011). Nonuniform cratering of the Moon and a revised crater chronology of the inner Solar System. *Icarus*, 214, 1–20. doi:10.1016/j.icarus.2011.03.010.
- Liakos, A., Bonanos, A. Z., Xilouris, E. M., Koschny, D., Bellas-Velidis, I., Boumis, P., Charmandaris, V., Dapergolas, A., Fytalis, A., Maroussis, A., & Moissl, R. (2020). NELIOTA: Methods, statistics, and results for meteoroids impacting the Moon. *Astronomy & Astrophysics*, 633, A112. doi:10.1051/0004-6361/201936709. arXiv:1911.06101.
- Madiedo, J. M., Ortiz, J. L., & Morales, N. (2018). The first observations to determine the temperature of a lunar impact flash and its evolution. *Monthly Notices of the Royal Astronomical Society*, 480, 5010–5016. doi:10.1093/mnras/sty1862. arXiv:1807.03193.
- Madiedo, J. M., Ortiz, J. L., Morales, N., & Cabrera-Caño, J. (2014). A large lunar impact blast on 2013 September 11. *MNRAS*, 439, 2364–2369. doi:10.1093/mnras/stu083. arXiv:1402.5490.

- Madiedo, J. M., Ortiz, J. L., Morales, N., & Cabrera-Caño, J. (2015a). MIDAS: Software for the detection and analysis of lunar impact flashes. *Planetary & Space Science*, 111, 105–115. doi:10.1016/j.pss.2015.03.018. arXiv:1503.07018.
- Madiedo, J. M., Ortiz, J. L., Morales, N., & Cabrera-Caño, J. (2016). Analysis of Lunar Impact Flashes Recorded During the Activity Period of the Lyrid Meteor Shower in 2013. In *Lunar and Planetary Science Conference* Lunar and Planetary Science Conference (p. 1124).
- Madiedo, J. M., Ortiz, J. L., Organero, F., Ana-Hernández, L., Fonseca, F., Morales, N., & Cabrera-Caño, J. (2015b). Analysis of Moon impact flashes detected during the 2012 and 2013 Perseids. *Astronomy & Astrophysics*, 577, A118. doi:10.1051/0004-6361/201525656. arXiv:1503.05227.
- Marchi, S., Chapman, C. R., Barnouin, O. S., Richardson, J. E., & Vincent, J. B. (2015). Cratering on Asteroids. In *Asteroids IV* (pp. 725–744). doi:10.2458/azu_uapress_9780816532131-ch037.
- Marchi, S., Massironi, M., Vincent, J. B., Morbidelli, A., Mottola, S., Marzari, F., Küppers, M., Besse, S., Thomas, N., Barbieri, C., Naletto, G., & Sierks, H. (2012). The cratering history of asteroid (21) Lutetia. *Planetary & Space Science*, 66, 87–95. doi:10.1016/j.pss.2011.10.010. arXiv:1111.3628.
- McNamara, H., Jones, J., Kauffman, B., Suggs, R., Cooke, W., & Smith, S. (2004). Meteoroid Engineering Model (MEM): A Meteoroid Model For The Inner Solar System. *Earth Moon and Planets*, 95, 123–139. doi:10.1007/s11038-005-9044-8.
- Moorhead, A. V., Egal, A., Brown, P. G., Moser, D. E., & Cooke, W. J. (2019). Meteor shower forecasting in near-Earth space. *Journal of Spacecraft and Rockets*, 56, 1531–1545. doi:10.2514/1.A34416. arXiv:1904.06370.
- Moser, D. E., Suggs, R. M., Swift, W. R., Suggs, R. J., Cooke, W. J., Diekmann, A. M., & Koehler, H. M. (2011). Luminous Efficiency of Hypervelocity Meteoroid Impacts on the Moon Derived From the 2006 Geminids, 2007 Lyrids, and 2008 Taurids. In

W. J. Cooke, D. E. Moser, B. F. Hardin, & D. Janches (Eds.), *Meteoroids: The Smallest Solar System Bodies* (pp. 142–154).

Nemtchinov, I. V., Shuvalov, V. V., Artemieva, N. A., Ivanov, B. A., Kosarev, I. B., & Trubetskaya, I. A. (1998). Light Impulse Created by Meteoroids Impacting the Moon. In *Lunar and Planetary Science Conference*. volume 29 of *Lunar and Planetary Science Conference*.

Neslusan, L., Svoren, J., & Porubcan, V. (1998). A computer program for calculation of a theoretical meteor-stream radiant. *Astronomy & Astrophysics*, *331*, 411–413.

Neukum, G., Ivanov, B. A., & Hartmann, W. K. (2001). Cratering Records in the Inner Solar System in Relation to the Lunar Reference System. *Space Science Reviews*, *96*, 55–86.

Ortiz, J. L., Aceituno, F. J., & Aceituno, J. (1999). A search for meteoritic flashes on the Moon. *Astronomy & Astrophysics*, *343*, L57–L60.

Ortiz, J. L., Aceituno, F. J., Quesada, J. A., Aceituno, J., Fernández, M., Santos-Sanz, P., Trigo-Rodríguez, J. M., Llorca, J., Martín-Torres, F. J., Montañés-Rodríguez, P., & Pallé, E. (2006). Detection of sporadic impact flashes on the Moon: Implications for the luminous efficiency of hypervelocity impacts and derived terrestrial impact rates. *Icarus*, *184*, 319–326. doi:10.1016/j.icarus.2006.05.002.

Ortiz, J. L., Madiedo, J. M., Morales, N., Santos-Sanz, P., & Aceituno, F. J. (2015). Lunar impact flashes from Geminids: analysis of luminous efficiencies and the flux of large meteoroids on Earth. *Monthly Notices of the Royal Astronomical Society*, *454*, 344–352. doi:10.1093/mnras/stv1921. arXiv:1511.07153.

Ortiz, J. L., Quesada, J. A., Aceituno, J., Aceituno, F. J., & Bellot Rubio, L. R. (2002). Observation and Interpretation of Leonid Impact Flashes on the Moon in 2001. *The Astrophysical Journal*, *576*, 567–573. doi:10.1086/341625.

- Ortiz, J. L., Sada, P. V., Bellot Rubio, L. R., Aceituno, F. J., Aceituno, J., Gutiérrez, P. J., & Thiele, U. (2000). Optical detection of meteoroidal impacts on the Moon. *Nature*, *405*, 921–923.
- Plescia, J. B., Robinson, M. S., Wagner, R., & Baldridge, R. (2016). Ranger and Apollo S-IVB spacecraft impact craters. *Planetary & Space Science*, *124*, 15–35. doi:10.1016/j.pss.2016.01.002.
- Robinson, M. S., Boyd, A. K., Denevi, B. W., Lawrence, S. J., McEwen, A. S., Moser, D. E., Povilaitis, R. Z., Stelling, R. W., Suggs, R. M., Thompson, S. D., & Wagner, R. V. (2015). New crater on the Moon and a swarm of secondaries. *Icarus*, *252*, 229–235. doi:10.1016/j.icarus.2015.01.019.
- Schmidt, R. M., & Housen, K. R. (1987). Some recent advances in the scaling of impact and explosion cratering. *International Journal of Impact Engineering*, *5*, 543–560.
- Schultz, P. H., Eberhardy, C. A., Ernst, C. M., A'Hearn, M. F., Sunshine, J. M., & Lisse, C. M. (2007). The Deep Impact oblique impact cratering experiment. *Icarus*, *191*, 84–122. doi:10.1016/j.icarus.2007.06.031.
- Schultz, P. H., Ernst, C. M., & Anderson, J. L. B. (2005). Expectations for Crater Size and Photometric Evolution from the Deep Impact Collision. *SSR*, *117*, 207. doi:10.1007/s11214-005-3383-7.
- Schultz, P. H., Hermalyn, B., Colaprete, A., Ennico, K., Shirley, M., & Marshall, W. S. (2010). The LCROSS Cratering Experiment. *Science*, *330*, 468. doi:10.1126/science.1187454.
- Schultz, P. H., Hermalyn, B., & Veverka, J. (2013). The Deep Impact crater on 9P/Tempel-1 from Stardust-NExT. *Icarus*, *222*, 502–515. doi:10.1016/j.icarus.2012.06.018.

- Sheward, D., Avdellidou, C., & Sefton-Nash, E. (2019). PyNAPLE: Automated Lunar Impact Flash Crater Detection. In *EPSC-DPS Joint Meeting 2019* (pp. EPSC-DPS2019–1032). volume 2019.
- Singer, K. N., McKinnon, W. B., Gladman, B., Greenstreet, S., Bierhaus, E. B., Stern, S. A., Parker, A. H., Robbins, S. J., Schenk, P. M., Grundy, W. M., Bray, V. J., Beyer, R. A., Binzel, R. P., Weaver, H. A., Young, L. A., Spencer, J. R., Kavelaars, J. J., Moore, J. M., Zangari, A. M., Olkin, C. B., Lauer, T. R., Lisse, C. M., Ennico, K., New Horizons Geology, G., Team, I. S. T., New Horizons Surface Composition Science Theme Team, & New Horizons Ralph and LORRI Teams (2019). Impact craters on Pluto and Charon indicate a deficit of small Kuiper belt objects. *Science*, *363*, 955–959. doi:10.1126/science.aap8628. arXiv:1902.10795.
- Steyaert, C. (1991). Calculating the solar longitude 2000.0. *WGN, Journal of the International Meteor Organization*, *19*, 31–34.
- Stooke, P. J. (2019). Identification of the SMART-1 spacecraft impact location on the Moon. *Icarus*, *321*, 112–115. doi:10.1016/j.icarus.2018.11.009.
- Strycker, P. D., Chanover, N. J., Miller, C., Hamilton, R. T., Hermalyne, B., Suggs, R. M., & Sussman, M. (2013). Characterization of the LCROSS impact plume from a ground-based imaging detection. *Nature Communications*, *4*, 2620. doi:10.1038/ncomms3620.
- Suggs, R. M., Moser, D. E., Cooke, W. J., & Suggs, R. J. (2014). The flux of kilogram-sized meteoroids from lunar impact monitoring. *Icarus*, *238*, 23–36. doi:10.1016/j.icarus.2014.04.032. arXiv:1404.6458.
- Sugita, S., Honda, R., Morota, T., Kameda, S., Sawada, H., Tatsumi, E., Yamada, M., Honda, C., Yokota, Y., Kouyama, T., Sakatani, N., Ogawa, K., Suzuki, H., Okada, T., Namiki, N., Tanaka, S., Iijima, Y., Yoshioka, K., Hayakawa, M., Cho, Y., Matsuo, M., Hirata, N., Hirata, N., Miyamoto, H., Domingue, D., Hirabayashi, M., Nakamura, T., Hiroi, T., Michikami, T., Michel, P., Ballouz, R. L., Barnouin, O. S., Ernst, C. M., Schröder, S. E., Kikuchi, H., Hemmi, R., Komatsu, G., Fukuhara, T.,

Taguchi, M., Arai, T., Senshu, H., Demura, H., Ogawa, Y., Shimaki, Y., Sekiguchi, T., Müller, T. G., Hagermann, A., Mizuno, T., Noda, H., Matsumoto, K., Yamada, R., Ishihara, Y., Ikeda, H., Araki, H., Yamamoto, K., Abe, S., Yoshida, F., Higuchi, A., Sasaki, S., Oshigami, S., Tsuruta, S., Asari, K., Tazawa, S., Shizugami, M., Kimura, J., Otsubo, T., Yabuta, H., Hasegawa, S., Ishiguro, M., Tachibana, S., Palmer, E., Gaskell, R., Le Corre, L., Jaumann, R., Otto, K., Schmitz, N., Abell, P. A., Barucci, M. A., Zolensky, M. E., Vilas, F., Thuillet, F., Sugimoto, C., Takaki, N., Suzuki, Y., Kamiyoshihara, H., Okada, M., Nagata, K., Fujimoto, M., Yoshikawa, M., Yamamoto, Y., Shirai, K., Noguchi, R., Ogawa, N., Terui, F., Kikuchi, S., Yamaguchi, T., Oki, Y., Takao, Y., Takeuchi, H. et al. (2019). The geomorphology, color, and thermal properties of Ryugu: Implications for parent-body processes. *Science*, *364*, 252–252. doi:10.1126/science.aaw0422.

Vincent, J.-B., Oklay, N., Marchi, S., Höfner, S., & Sierks, H. (2015). Craters on comets. *Planetary & Space Science*, *107*, 53–63. doi:10.1016/j.pss.2014.06.008.

Walsh, K. J., Jawin, E. R., Ballouz, R. L., Barnouin, O. S., Bierhaus, E. B., Connolly, H. C., Molaro, J. L., McCoy, T. J., Delbo, M., Hartzell, C. M., Pajola, M., Schwartz, S. R., Trang, D., Asphaug, E., Becker, K. J., Beddingfield, C. B., Bennett, C. A., Bottke, W. F., Burke, K. N., Clark, B. C., Daly, M. G., DellaGiustina, D. N., Dworkin, J. P., Elder, C. M., Golish, D. R., Hildebrand, A. R., Malhotra, R., Marshall, J., Michel, P., Nolan, M. C., Perry, M. E., Rizk, B., Ryan, A., Sandford, S. A., Scheeres, D. J., Susorney, H. C. M., Thuillet, F., Lauretta, D. S., & Team, O.-R. (2019). Craters, boulders and regolith of (101955) Bennu indicative of an old and dynamic surface. *Nature Geoscience*, *12*, 242–246.

Xilouris, E. M., Bonanos, A. Z., Bellas-Velidis, I., Boumis, P., Dapergolas, A., Maroussis, A., Liakos, A., Alikakos, I., Charmandaris, V., Dimou, G., Fytalis, A., Kelley, M., Koschny, D., Navarro, V., Tsiganis, K., & Tsinganos, K. (2018). NELIOTA: The wide-field, high-cadence, lunar monitoring system at the prime focus of the Kryoneri telescope. *Astronomy & Astrophysics*, *619*, A141. doi:10.1051/0004-6361/201833499. arXiv:1809.00495.

Yanagisawa, M., & Kisaichi, N. (2002). Lightcurves of 1999 Leonid Impact Flashes on the Moon. *Icarus*, 159, 31–38. doi:10.1006/icar.2002.6931.

Yanagisawa, M., Ohnishi, K., Takamura, Y., Masuda, H., Sakai, Y., Ida, M., Adachi, M., & Ishida, M. (2006). The first confirmed Perseid lunar impact flash. *Icarus*, 182, 489–495. doi:10.1016/j.icarus.2006.01.004.